JGR Earth Surface

RESEARCH ARTICLE
10.1029/2022JF006715

Deriving Debris-Flow Dynamics From Real-Time Impact-Force Measurements

Yan Yan[1,2,3], Hui Tang[4], Kaiheng Hu[5,6], Jens M. Turowski[3], and Fangqiang Wei[5,6]

[1]Key Laboratory of High-Speed Railway Engineering, MOE/School of Civil Engineering, Southwest Jiaotong University, Chengdu, China, [2]Institute of Geographic Sciences and Natural Resources Research, Chinese Academy of Sciences, Beijing, China, [3]Section 4.6: Geomorphology, German Research Centre for Geosciences (GFZ), Potsdam, Germany, [4]Section 4.7: Earth Surface Process Modelling, German Research Centre for Geosciences (GFZ), Potsdam, Germany, [5]Key Laboratory of Mountain Hazards and Earth Surface Processes, Chinese Academy of Sciences, Chengdu, China, [6]Institute of Mountain Hazards and Environment, Chinese Academy of Sciences, Chengdu, China

Abstract Understanding the impact forces exerted by debris flows is limited by a lack of direct field measurements and validated numerical models. In this study, we use real-time impact-force measurements and field observations of debris flows recorded by a sensor network in Jiangjia Ravine, China, to quantify the impact-force distribution of natural debris flows. We observed one debris flow event during and after a storm on 25 August 2004, including 42 short-duration surges and seven long-duration surges, and impact-force signals were successfully recorded for 38 surges. Our observed debris flows comprise high-viscosity laminar flows with high sediment concentration and frequent solid-to-solid interactions. We identified a large magnitude (up to 1 kN), high-frequency (greater than 1 Hz) fluctuating component of the impact force that we interpret as solid particle impact on the sensors. The variability of particle impact forces increases with the mean impact force. Our results show that a log-logistic distribution can describe the probability density distribution of impact forces. Solid-dominated surges and fluid-dominated intersurge flows have similar impact-force distributions, but surges usually have heavy tails. We created a dimensionless number to describe the impact force and correlated it against existing dimensionless parameters. Finally, we develop a simple particle impact model to understand the relationship between flow dynamics and the impact force inside debris flows that could be applied to improve debris-flow flume experiments and design debris-flow hazard mitigation measures.

Plain Language Summary Debris flows are fast-moving mixtures of dirt and water that can cause huge damage to buildings and infrastructures and harm people. For effective hazard protection, we need to understand the impact forces exerted by debris flows. In this study, we measured impact forces at the high temporal resolution of 49 debris-flow surges during and after a storm on 25 August 2004, recorded by a sensor array in Jiangjia Ravine, southwestern China. We develop statistical descriptions of the mean and the variability of the force and derive a relationship between flow dynamics and the impact force using a simple particle impact model. Our results could be applied to improve the future design of debris-flow hazard mitigation measures.

Key Points:

- Log-logistic distribution is a good fit for debris-flow impact force probability density functions
- Debris-flow surges and intersurge flows have similar impact force distribution, but surges usually have heavy tails
- A simple particle impact model can explain the debris-flow impact force signal

Supporting Information:

Supporting Information may be found in the online version of this article.

Correspondence to:

H. Tang and K. Hu,
htang@gfz-potsdam.de;
khhu@imde.ac.cn

Citation:

Yan, Y., Tang, H., Hu, K., Turowski, J. M., & Wei, F. (2023). Deriving debris-flow dynamics from real-time impact-force measurements. *Journal of Geophysical Research: Earth Surface*, *128*, e2022JF006715. https://doi.org/10.1029/2022JF006715

Received 4 MAY 2022
Accepted 7 MAR 2023

1. Introduction

Debris flows are common in steep alpine environments, with the potential to travel long distances, severely damage objects in their path, and cause significant fatalities (Thouret et al., 2020). Dowling and Santi (2014) reported around 77,800 fatalities between 1950 and 2011 in 213 debris-flow events, which makes debris flow one of the most destructive natural hazards after earthquakes and floods. Debris-flow impacts on buildings and infrastructure have been examined in several studies (e.g., Bugnion, McArdell, et al., 2012; Cui et al., 2015; Gao et al., 2017; Hübl et al., 2009; Iverson, 1997; Thouret et al., 2020; Zeng et al., 2015). Experiments measuring debris-flow impact pressure have been conducted in small-scale laboratories and large-scale natural environments (e.g., Proske et al., 2018; Scheidl et al., 2013). Medium- to small-scale laboratory experiments have enabled engineers to learn how a debris flow hits an obstacle, how it varies, and to quantify its mechanical impacts on a vertical wall (Zhao et al., 2018), ridge piers (D. Wang et al., 2018), or barriers (Song et al., 2019). Most studies only consider the peak impact force rather than the range of impact forces, as it is assumed to be most relevant for causing damage (e.g., Cui et al., 2015; Thouret et al., 2020; S. Zhang et al., 2019). In practice, the maximum estimated pressure or force from debris flow is commonly used to indicate the peak energy when

designing prevention and control measures for debris flow (e.g., Kwan, 2012; Kwan & Cheung, 2012). However, this approach is only concerned with a single, local, instantaneous pressure, which gives a limited picture of the impact of debris flows. Not only does the peak impact bring damage by debris flow, but other smaller impacts can also cause damage, implying that the distribution of debris flow impact forces is relevant for damage prediction. Thus, if the relationship between debris flow dynamics and the distribution of impact forces can be systematically described, control measure design and hazard assessment can be correspondingly improved.

The basal force is one of the important components of debris flow impact force, and the basal forces generated by debris flows can be measured using force plates on the channel floor or check dam and have been used to study debris-flow properties and bed erosion mechanisms (e.g., Berger et al., 2011a; Berti et al., 2000; Cui et al., 2018; Kean et al., 2015; McArdell, 2016; McArdell et al., 2007; McCoy et al., 2013). Some laboratory experiments (e.g., Gardel et al., 2009) and numerical modeling results (e.g., Lois et al., 2007) indicate that the probability density function (PDFs) of particle-bed contact forces has an exponential tail. In contrast, McCoy et al. (2013) found the PDFs of normal basal forces for debris flow at the Chalk Cliffs, USA, followed a generalized Pareto distribution, which has a higher probability of large forces. This disparity is probably due to differences in rheology and the concentration of large particles. Similarly, Hsu et al. (2014), based on laboratory flume experiments, suggested that normal basal forces greater than the mean can be described with a generalized Pareto distribution. However, the impact forces inside natural debris flows and how they change with debris-flow magnitude are still little known, leaving several unanswered questions. For example, what is the force distribution of natural debris flow impact on hard structures? Is there a relationship between force distribution and flow dynamics? Which dimensionless number can be used to quantify the impact force of debris flow Can we represent the impact force by a simple particle impact model? Which aspects of impact force experiments and simulations apply to full-scale debris flows in natural settings?

Debris flows comprise a fluid phase and a solid phase (Iverson, 1997), and their interactions reflect intrinsic properties and flow dynamics. In addition, observations show that debris-flow-related damage may be caused by both fluid and particle impact (e.g., Thouret et al., 2020; D. Wang et al., 2018), and field measurements in natural debris flows show that impact forces from large particles are several orders of magnitude larger than those from the fluid phase (K. Hu et al., 2011). Hydrodynamic, hydrostatic, and particle collision forces contribute to debris flow impact forces (e.g., Lei et al., 2018; D. Wang et al., 2018). Various approaches have been taken to conceptualize and analyze each of these components in the field and laboratory (e.g., H. Hu et al., 2020; Iverson et al., 2010; Thouret et al., 2020). Although these approaches can reproduce and estimate debris-flow impacts and damages to some extent, the field-scale relationship between particle impact properties and flow dynamics remains unquantified. This is because the large excursions of impact force magnitudes from the mean values (e.g., 170 kN/m^2 in Figure 8b of K. Hu et al. (2011)) scale with variables characterizing flow dynamics (e.g., the discharge fluctuation is 2,000 m^3/s in Li et al. (2015)), and their frequency-magnitude distribution remains poorly quantified, especially in natural debris flows with broad grain size distributions. Hence, understanding the impact mechanics of debris flows and encoding their flow dynamics is essential for discerning controls on impact damage and their influence on channel evolution.

Debris flow dynamics arise through the interaction of several forces, including inertial force, frictional resistance, and pore pressure, which may decrease the resistance force (Iverson, 1997). Several dimensionless numbers have been proposed to characterize and analyze debris-flow dynamics and the forces acting on solid and fluid phases. The Savage number represents the inertial force of the solid phase over effective shear stress, which is the ratio between inertial collision forces and solid contact friction in the solid phase of saturated flows (Iverson, 1997). The friction number compares the solid-phase contact friction to the fluid-phase viscous resistance, representing the rheological characteristics of solid-fluid mixtures in debris flow (Iverson, 1997). The Bagnold number is a ratio between inertial force and viscous force and distinguishes viscous-force-dominated flow and inertial-force-dominated flow (Hunt et al., 2002). The mass numbers represent the ratio between the solid phase's inertial forces and those of the fluid phase (Iverson, 1997). The particle Reynolds number was developed for mixed grain flows and compares the inertial and viscous forces at the particle scale (Iverson, 1997). The Froude number represents the ratio between inertial and gravitational forces and can differentiate critical and subcritical flow (Heller, 2011). Dimensionless numbers are a simplified method for quantifying debris-flow dynamics and are compared among small-scale experiments, direct field measurements, and numerical simulations.

Many field studies have used a combination of flow depth, channel geometry, and velocity measurements to characterize debris-flow dynamics (e.g., Bel et al., 2017; Gregoretti et al., 2016; Okano et al., 2012), but very few studies have attempted to determine the internal flow of a debris flow. A recent exception is a study by Nagl

et al. (2020), who used conductivity sensors to determine velocity profiles in two natural debris flows. They found that the velocity profiles in debris flow varied from front to tail and between flows at their study sites. Some simple numerical models based on indirect measurements, such as using the seismic signals of seismic stations for dynamics inversion (Yan, Cui, Huang, et al., 2022), or the seismic signals generated by bed-particle interactions, have been proposed to reconstruct debris-flow dynamics (e.g., Farin et al., 2019; Kean et al., 2015; Lai et al., 2018). Kean et al. (2015) found that the spectral power of the seismic signal systematically increased as the debris flow entrained bed sediment. Lai et al. (2018) were able to estimate boulder sizes, debris-flow speed, and distance from amplitude and frequency characteristics of seismic data. Farin et al. (2019) developed a process-based model for the high-frequency spectral distribution of seismic signal power generated by debris flows based on four regions (flow body, coarser-grained snout, snout lip, and dilute front) with different controlling mechanisms. These models can predict normal basal force and seismic signals, but the relationships between basal force, impact force, and debris-flow dynamics are unclear (e.g., Z. Zhang, Walter, McArdell, Chmiel, et al., 2021; Z. Zhang, Walter, McArdell, de Haas, et al., 2021). It would be useful to develop a simple model to estimate the variability of debris-flow properties in the vertical direction (such as flow depth, vertical velocity profiles, and dimensionless numbers) based on real-time impact force measurement.

In this study, we investigate the characteristics of impact forces and flow dynamics inside natural debris flows using comprehensive field measurements, including real-time impact force measurements, with signal and dimensional analysis. First, we present impact-force measurements from 38 debris flow surges from Jiangjia Ravine, analyze them in both the time and frequency domain, and determine the essential characteristics of probability density distribution (e.g., type and parameters). Then, we derive various debris-flow dimensionless numbers, investigate the relationship between these numbers and impact-force signals, and compare them with examples from other basins and flume experiments to assess the general physical mechanisms. To quantify impact pressure, we define a new dimensionless number (non-dimensional impact pressure, P^*) and explore its correlation with other dimensionless numbers. Finally, we develop a simple particle impact model to quantify high-frequency impact-force signals and combine the data set with numerical analysis to derive dynamics in the vertical profile and interpret the impact-force signal. A key advantage of using such empirical relationships with a simple particle impact model for control measure design and hazard assessment is that they can be more universally applied in other areas, even without historical data on debris flows.

2. Methodology

2.1. Study Site

Our study site, Jiangjia Ravine, is located on the right bank of the Xiaojiang River, Yunnan, China (Figure 1a). The total drainage area is about 48.5 km^2, and the main channel is approximately 13.9 km long. The bedrock, mainly composed of slate and dolomite, is usually highly weathered to fine particles that provide abundant sediment sources for debris flows (Cui et al., 2005). Sediment generally accumulates in the channel via landslides, dry ravel, and rockfall from the steep hillslope during cold periods (Cui et al., 2005). The study site is subject to the most frequent debris-flow activity in Southwest China, with an average of about eight debris-flow events per year (Cui et al., 2005). Debris flows usually occur during summer rainstorms from late May to September when runoff concentrates in channels and mobilizes sediment (S. Zhang et al., 2020). A typical debris-flow event at Jiangjia Ravine consists of multiple steep-front, high-viscosity, coarse-grained surges separated by water-rich intersurge flows. The debris-flow surge front surface usually contains a large amount of coarse-grained debris and has a consistency such that material launches into the air when it impacts an obstacle. The debris-flow surge commonly has a sediment concentration greater than 40%, while it is generally between 20% and 40% for intersurge flow; the latter flow is termed debris flood or hyperconcentrated flow in the literature (e.g., Cui et al., 2005; McCoy et al., 2013). Here, we consider a debris-flow event composed of 42 short-duration surges and seven long-duration surges (Tables S1 and S2 in Supporting Information S1). More details on the study site can be found in Cui et al. (2005) and K. Hu et al. (2011).

2.2. Field Measurements and Observations

Field monitoring focused on two observation sections in the main channel of Jiangjia Ravine (130 m, short green lines in Figure 1a). The monitoring system comprised three rain gauges, three impact force sensors, one

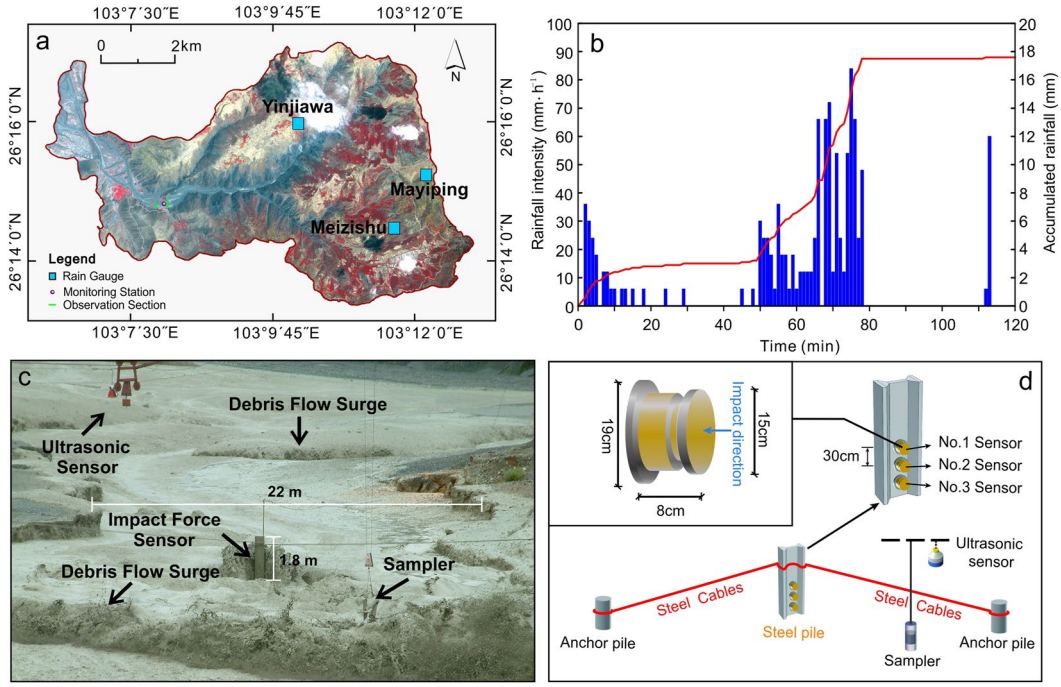

Figure 1. Study site location and monitoring set-up: (a) Satellite image of the Jiangjia Ravine, Yunnan, China, showing the location of the monitoring station, observation sections, and rain gauges (Adapted from Li et al. (2015)); (b) One-minute rainfall intensity (blue) and accumulated rainfall (red) at Mayiping rainfall gauge for the storm of 25 August 2004, starting at 11:20 a.m. local time. The location is shown in panel (a); (c, d) Monitoring station set-up and detail of impact force sensors.

ultrasonic sensor for the flow stage, and one sampler to collect sediment from the debris-flow surface (Figures 1c, 1d, and 2). The monitoring system also included a coarse grain sampler comprising a 61 cm high cylinder with an 18 cm inner diameter (Figure 2a). All sediment samples were collected from the debris-flow surface right after the surge front (Figure 2b); initially, the sampler was placed close to the bed and then raised using hanging cables and a pulley after the flow had passed (Figure 2b). Theoretically, the sampler could collect grains as large as 18 cm, but grains over 10 cm were rarely collected in practice. Sample bulk density was estimated using the mass-to-volume ratio. We used two synchronized stopwatches to manually record the arrival time of surge fronts at the two observation sections (Figure 1a). We estimated the travel time between the two sections based on the time difference to calculate the average velocity U_m. Three bucket gauges recorded rainfall every minute during a monitored storm event on 25 August 2004 (Figure 1a). The event began at 11:24 and ended at 13:14 local time, with 17.6 mm total rainfall at the top of the basin (Mayiping station) and maximum one-minute rainfall intensity

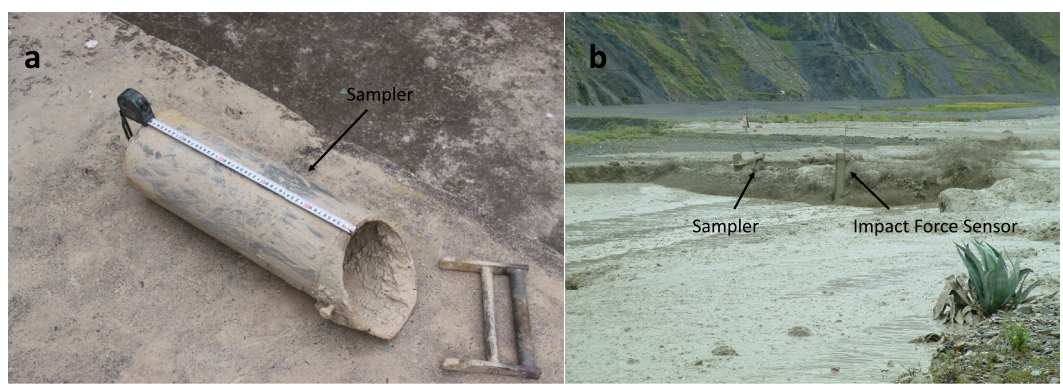

Figure 2. (a) Details for sediment sampler and (b) the location of sediment sampler and impact force sensor. Sediment samples for the debris-flow surface were collected a few meters downstream from the impact sensor and right after the debris-flow front to protect the sampler. We collected all sediment particles up to 18 cm.

of about 83 mm hr^{-1} (Figure 1b). The debris-flow event started at 12:40 local time. We observed one debris flow event with 49 surges during and after the storm, including 42 short-duration surges and seven long-duration surges with no distinct surge front at the beginning and end of the event (Tables S1 and S2 in Supporting Information S1). Impact-force signals were successfully recorded for 38 surges (No. 3–42, excluding No. 37 and 41) from 12:56 until 14:55 local time. Additional details regarding the monitoring equipment and methods can be found in K. Hu et al. (2011).

Bulk sediment samples were collected from the flow surface of the 10th, 21st, and 30th debris-flow surges right after the flow peak. Their grain size distributions and bulk densities were determined in the lab (see Figure 4 in K. Hu et al. (2011) for details and Figure S16 in Supporting Information S1). Based on the standard sieve method (Cui et al., 2005), the median grain size (D_{50}) of the three bulk samples, excluding larger clasts and boulders, was about 8–10 mm with wide distributions that spanned over six orders of magnitude (Figure S16 in Supporting Information S1). Bulk densities ranged from 1,600 to 2,300 kg m^{-3}. Sediment concentration (C), a key input parameter of the particle impact model (refer to Section 2.5 Simplified Particle Impact Model), constrained from in situ field measurements based on the ratio of the volume of solid material in the sample and the total sample volume. The flow stage was measured by an ultrasonic sensor suspended over the channel near the impact force sensors (Figure 1c). The datum for stage measurements was the bottom of the impact force plate; thus, when no sediment was deposited on the bottom, the flow stage was bed-normal flow depth. Due to erosion and deposition during debris-flow events, the thickness of stationary bed sediment beneath the flow is not known precisely as a function of time. During each surge, we roughly estimated flow depth (H_m) from the maximum height difference between the flow surface and the pre-debris-flow channel bottom using the ultrasonic sensor.

All impact force instrumentation was located at the downstream station. Three impact sensors of 15 cm diameter, designed and made by the Facility Design and Instrumentation Institute, China Aerodynamics Research and Development Center, were installed vertically on the pile front at a uniform spacing of 30 cm (Figure 1d). The lowermost sensor was about 65 cm above the pre-debris-flow event channel bed. The impact force sensor has a response time of less than 1 ms, a maximum frequency of 8 kHz, a maximum value of 100 kN, and a minimum value of 0.3 N, with an accuracy of about 3%. The sampling frequency was set to 2 kHz. The natural frequency of the impact force sensor is above 200 Hz. The median diameter of grains is equal to D_{50} and the maximum flow velocity (12 m s^{-1}), which means that the duration of the Hertzian collision is around 0.04 ms. Therefore, we assumed each force measurement approximates an instantaneous measure of the force on the plate surface. As plate area increases, the hydrostatic pressure acting on the plate increases, which increases the time-averaged mean normal force on the plate. We expect that grain-scale dynamics are strongly controlled by solid phase in debris flows, and a larger plate area permits more particles to contact the plate. If particle-plate contact forces are spatially uncorrelated, then fluctuation amplitude relative to the time-averaged mean force will decrease as contact forces are spatially averaged. Therefore, we chose a plate size close to the diameter of large particles in the flow. Debris-flow dynamics are sensitive to location and whether flow has been disrupted; hence, flow dynamics measured by our plate should represent that developed mid-channel and within a supercritical flow.

2.3. Impact-Force Signal Processing and Analysis

The impact-force signals from the sensor require processing before analysis; impact-force signals from debris flow are usually non-linear and non-stationary, with harmonics of multiple frequency points, significant fluctuation, and background noise. Using the code of Y. Wang et al. (2014) with zero added noise, empirical mode decomposition (EMD) was applied to separate vibration from harmonics and remove noise from the impact vibration signal (Boudraa & Cexus, 2007; N. E. Huang & Wu, 2008; Yan, Cui, Guo, et al., 2020; Yan, Cui, Tian, et al., 2020). The prominent noise of concern in our data comes from the same-frequency harmonics of the sensor, most of which are very high-frequency (>180 Hz). EMD allows us to remove these high-frequency components by decomposing the signal into intrinsic mode functions (IMFs) with spectral content at incrementally decreasing frequencies, the number of IMF is determined by the EMD processing process adaptively, and its range is usually 7–15. We exclude the first 3 or 4 IMFs from the signal, as Chang and Liu (2011) shows to reduce noise without causing signal phase delay or distortion. For the impact force, the noise of the middle sensor is stronger than the other two sensors. Therefore, the number of IMF noise components used by the middle sensor is four. The IMF noise component used by the data of the top and bottom sensors is three. The number of IMF is selected manually according to removing noise while keeping useful signal components as much as possible. Several groups of

typical filtering results with different noise numbers are supplemented in Figures S18–S25 in Supporting Information S1. The short-time Fourier transform method (Yan, Cui, Guo, et al., 2020; Yan, Cui, Tian, et al., 2020) was used to transform the impact-force signal into a joint time-frequency domain to quantify the characteristics of the force signal. The power of each frequency that corresponds to a given debris-flow period can be calculated based on the power spectral density (PSD) of the vibration signal as a function of frequency (f) (Oppenheim et al., 1997):

$$PSD(f) = |\tilde{F}(f)|^2/\Delta f, \tag{1}$$

where $\tilde{F}$ is the Fourier transform of the impact force $F(t)$, Δf is frequency resolution which is equal to $1/T$ (T is window length). We used the Welch method to calculate PSDs. The Welch estimate method is a windowed mean periodogram method in PSD calculation, which can improve the resolution of spectral estimation and reduce energy leakage (Welch, 1967). We used a window length of 2,048 data points and an 80% overlap of the two windows, which is 1,638 data points. The impact force ($F(t)$) as a function of time can also be separated into a moving median of the impact force ($\overline{F}(t)$) and a fluctuating component of the impact force ($\hat{F}(t) = |F(t) - \overline{F}(t)|$). $\overline{F}(t)$ is set largely by hydro-pressure (McCoy et al., 2013). In contrast, through the time-domain moving-window-median filter with a 400 points window (0.2 s or 5 Hz) set by grain-scale processes, the median and fluctuating components of the impact-force signal are separated to obtain $\hat{F}(t)$.

The fluctuating component is usually high frequency and is difficult to define objectively; in this study, we considered all signals above 5 Hz as the high-frequency component. The relative impact energy transferred from the impact to the sensor was calculated using the formula:

$$E = \sum_{i=1}^{N} \frac{(1-e)F(i)\Delta t U_m}{2}, \tag{2}$$

where e is a constant coefficient of restitution, our impact sensor is stainless steel plate ($e \approx 0.7$), Δt is the sampling interval, $F(i)$ is the ith sampling value of impact force, U_m is averaged flow velocity.

We analyzed probability density functions (PDFs) for impact force to determine their distribution shape and understand how the distributions change across debris-flow events and measurable flow properties. Our goal in this analysis was to determine which flows have the potential to generate the large magnitude impact forces more likely to cause damage. We separated the force data into populations based on the time of each event. First, the impact forces of all the surges and intersurges were normalized by the median impact force to remove the influence of variability in $\overline{F}(t)$ on the distribution of $F(t)$ and to isolate the influence of grain-scale processes. We normalized each force measurement $F(t)$ by its concurrent $\overline{F}(t)$ (McCoy et al., 2013):

$$Fn(t) = \frac{F(t)}{\overline{F}(t)}. \tag{3}$$

A single master population was created by combining force plate measurements from all events. They were separated into two groups (debris-flow surge and water-rich intersurge) based on the magnitude and shape of the impact-force signals, following Cui et al. (2015). Similar to stage data (Kean et al., 2013; Tang et al., 2019), we identified debris-flow surges as asymmetric shapes in the impact-force signal, with an abrupt rise followed by a slow decline (Figure 3 and Figures S1–S4 in Supporting Information S1). The debris-flow surge group includes measurements with high-magnitude impact force under relatively deep flow. The intersurge flow group contains measurements from the water-rich flow between two surges when the impact force is less than 10% of the peak (Cui et al., 2015).

To aid the quantitative comparison of flow dynamics, we calculated PDFs for measurements from the debris-flow surge period, the water-rich intersurge period, and the entire debris-flow period. We tested six distributions (exponential, gamma, generalized Pareto, Nakagami, normal, and log-logistic), which have been used in the literature to fit PDFs with maximum likelihood optimization (e.g., Hsu et al., 2014; McCoy et al., 2013), and evaluated them using the residual sum of squares (RSS). The RSS, which emphasizes the difference between the fitted distribution and the original data, is typically used to compare the statistical goodness of fit (Draper & Smith, 1998). We determined RSS by

$$RSS = \sum_{i=1}^{N} (y(Fn(i)) - f(Fn(i)))^2, \tag{4}$$

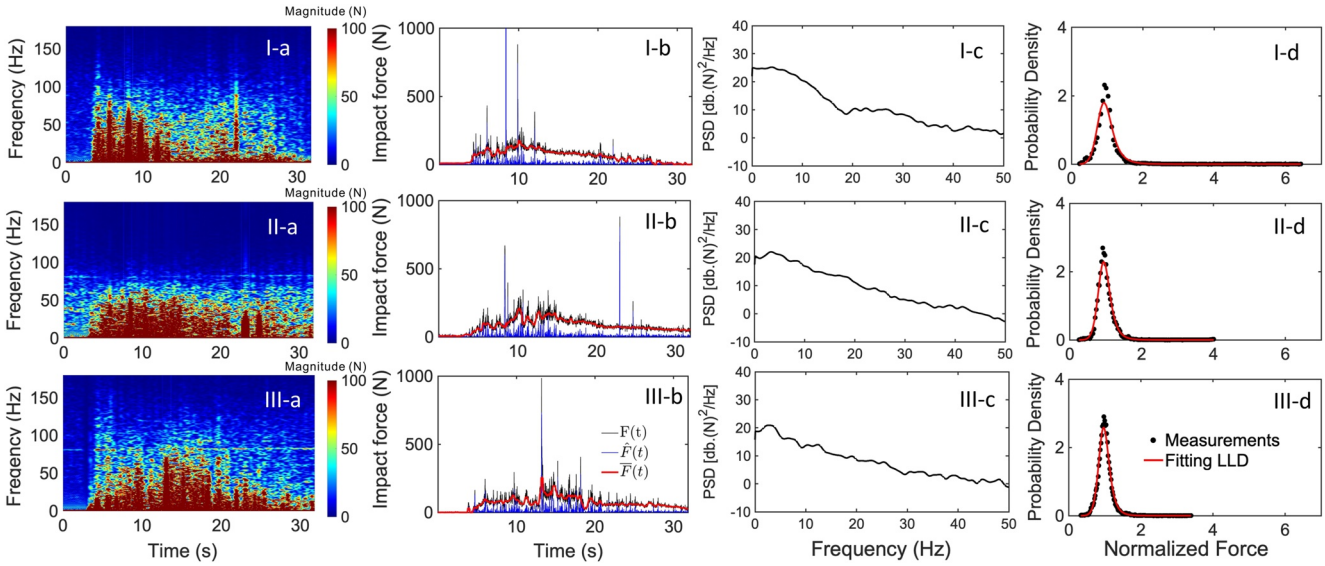

Figure 3. Summary of impact-force signals for the 19th surge (I-top sensor; II-middle sensor; and III-bottom sensor). (a) Power spectrum of the impact-force signal by short-time Fourier transformation; Most signals from impact force sensor are below 100 Hz for the 19th surge. (b) Time sequence of total impact force, $F(t)$, fluctuating component, $\hat{F}(t)$, mean impact force, $\overline{F}(t)$; The total impact force can be 50 times larger than mean impact force as shown in (I-b). (c): Power spectral density (PSD) for the entire impact-force signal ($F(t)$); The highest PSD, in terms of frequency, locates at the low-frequency part (<5 Hz). (d): Probability density functions of normalized impact-force measurements (black dots) and fitted log-logistic distribution (LLD) (red line). The LLD fits well for all impact-force measurements from three sensors. The impact-force measurements from the top sensor have shown apparent heavy tails above two.

where $y(Fn(i))$ is the ith value of the probability to be predicted and is an empirical distribution function, $Fn(i)$ is the ith value of the normalized impact force, and belongs to a cumulative distribution function, and $f(Fn(i))$ is the value at $Fn(i)$ of the best-fit cumulative distribution function. A perfect fit will give an RSS of zero (Tables S3–S7 in Supporting Information S1). The probability density for the log-logistic distribution (LLD), which fits best for impact forces, can be written as:

$$PDF(Fn,\mu,p)=\frac{1}{pe^{\mu}}\frac{(Fne^{-\mu})^{1/p-1}}{\left[1+(Fne^{-\mu})^{1/p}\right]^{2}}. \quad (5)$$

p is a shape parameter ($p>0$), but for $0<p<1$, a mean of the distribution does not exist, so here $p>1$. The distribution is unimodal when $p>1$, and its dispersion decreases as p increases (Ashkar & Mahdi, 2006). The scale parameter μ is related to the median, which is equal to e^{μ}. We also used the Kolmogorov-Smirnov test (KS-Test) (Stephens, 1974) to check the similarity between distributions from the surge and intersurge flow groups within each event. We assume the two distributions are similar when the Kolmogorov-Smirnov statistic is greater than 0.05.

2.4. Dimensionless Analysis

We used seven dimensionless numbers to give insights on simplified debris-flow dynamics and investigate the role of flow dynamics on impact-force distribution: dimensionless flow discharge (Q_*), Froude number (N_{Fr}), Savage number (N_{Sa}), Bagnold number (N_{Ba}), mass number (N_m), friction number (N_f), and particle Reynolds number (N_{Re}) (Bagnold, 1954; Iverson, 1997; Iverson & Vallance, 2001; Savage & Hutter, 1989; Zhou & Ng, 2010). Each dimensionless number is well-defined and has been applied widely in previous experimental and field-based research (Bagnold, 1954; Iverson, 1997; Iverson & Vallance, 2001; Savage & Hutter, 1989). We compared the dimensionless numbers derived from our study with experimental data reported in Lanzoni et al. (2017) and field data from other basins in the literature (Arattano & Franzi, 2004; Badoux et al., 2009; Bennett et al., 2014; Berger et al., 2011b; Berti et al., 1999; Chou et al., 2013; Coe et al., 2008; Marchi et al., 2002; McCoy et al., 2010, 2013; Okano et al., 2012; Suwa et al., 2009). Below we briefly define and describe each dimensionless number. The

dimensionless flow discharge (Q_*) is estimated from the flow discharge per unit width and the sediment grain size (Parker, 1979; Parker et al., 2007):

$$Q_* = \frac{U_m H_m}{\sqrt{g D_{50}^3}}, \tag{6}$$

where H_m is flow depth, U_m is averaged flow velocity, g is the gravitational acceleration. We constrained the median grain size, D_{50}, based on particle size analyses from three samples. We use 8 mm as D_{50} for 21 surges at the first part of the event and 10 mm as D_{50} for rest of the surges. The Froude number (N_{Fr}) is defined as:

$$N_{\mathrm{Fr}} = \frac{U_m}{\sqrt{g H_m}}. \tag{7}$$

The Froude number reflects the wave-making resistance in free-surface flow and can distinguish subcritical ($N_{\mathrm{Fr}} < 1$), critical flow ($N_{\mathrm{Fr}} = 1$), and supercritical flow ($N_{\mathrm{Fr}} > 1$). The Savage number (N_{Sa}) represents the ratio between the inertial and quasi-static stresses associated with collisions and long-lasting contacts of sediment grains (Savage & Hutter, 1989):

$$N_{\mathrm{Sa}} = \frac{\rho_s D_{50}^2 \gamma^2}{\sigma_e}, \tag{8}$$

where ρ_s is the density of sediment, and γ is the shear rate, which can be estimated as U_m/H_m. σ_e represents the effective normal basal stress equal to $\sigma - P$. σ is the normal compressive stress ($\rho g h \cos(\theta)$, where θ is channel gradient), and P is the pore fluid pressure ($\rho_f g h \cos(\theta)$); these two parameters are calculated based on the measured data. Based on several experiments (Savage & Hutter, 1989), grain collision stresses prevail over the grain friction stresses in granular flows when N_{Sa} exceeds about 0.1 (Iverson, 1997). The Bagnold number, N_{Ba}, (Bagnold, 1954) is the ratio between the inertial and quasi-static stresses associated with collisions and viscous fluid stresses:

$$N_{Ba} = \frac{\lambda^{1/2} \rho_s D_{50}^2 \gamma}{\mu_f}, \tag{9}$$

where λ is the linear concentration and equal to $C^{1/3} / \left(C_{\max}^{1/3} - C^{1/3} \right)$. C is the bulk sediment concentration. $C_{\max}$ is the closest packing sediment concentration and is equal to 0.65. μ_f is the viscosity of the interstitial fluid. μ_f of each surge can be obtained by rheological experiments, but here it is assumed to be 0.1 kg m^{-1} s^{-1}. The N_{Ba} can help distinguish the dominant model of momentum transport in a two-phase flow: large values of N_{Ba} (>200) indicate that grain collision dominates viscous drag stress (Iverson, 1997). A collisional regime ($N_{\mathrm{Sa}} > 0.1$ and $N_{\mathrm{Ba}} > 450$) prevails in the laboratory-generated debris flows and those observed at the field. According to Armanini et al. (2005), the transition from a frictional to a collisional behavior is also controlled by the viscosity of the interstitial fluid and occurs for N_{Ba} about 1,000. The mass number N_m (Iverson & Vallance, 2001) represents the ratio of inertia force between solid and slurry in the debris-flow mixture:

$$N_m = \frac{C \rho_s}{(1 - C) \rho_f}, \tag{10}$$

where ρ_s is density of water. A value of N_m greater than one suggests that solid grain dynamics dominate momentum transport and that an increase in sediment concentration increase N_m. N_f is the friction number (Iverson, 1997), and the ratio between the Bagnold number and Savage number, which indicates the importance of collision and represents the inertial and quasi-static stresses associated with long-lasting contacts and viscous fluid stresses:

$$N_f = \frac{\lambda^{1/2} \sigma_e}{\gamma \mu_f}. \tag{11}$$

Large values of N_f suggest that frictional shear stresses tend to exceed viscous shear stresses. N_{Re} is the particle Reynolds number (Iverson, 1997) and is the ratio between the Bagnold number and mass number, which indicates the role of viscous drag associated with solid-fluid interactions:

$$N_{\mathrm{Re}} = \frac{\rho_f D_{50}^2 \gamma}{\mu_f}. \tag{12}$$

The particle Reynolds number describes the turbulence magnitude within a fluid and quantifies the degree of turbulence at the particle scale. The seven dimensionless numbers and sediment concentration represent many degrees of freedom to investigate the first order of debris-flow dynamics (Figure 5).

In addition to the existing dimensionless number, we aim to establish a new dimensionless number to characterize debris-flow impact pressure quantitatively. The size of the sensor determines the area of the impact force, so in order to uniformly characterize the impact force, we determined that the new number should be based on pressure rather than force. Force is proportional to the change rate of the impulse; particle pulse depends on mass and impact velocity. Mass scales with the product of density and volume. Therefore, particle density and grain diameter are relevant parameters. We assume that impact velocity scales with the averaged flow velocity (U_m). We considered two approaches to create the new dimensionless number to describe debris flow impact pressure. The first one is based on the viscous flow Bernoulli theorem, where impacts are altered by viscous damping. The gain in kinetic energy due to loss of height is matched by energy loss to heat due to friction. The second method assumes that surface and bed effects are not negligible, so we need to incorporate flow depth (H_m) and height of the sensor above the bed (h), which leads to a particle Reynolds number approach. For the Bernoulli approach, fluid density was used to describe debris-flow impact pressure, while debris-flow density (mixture of particles and slurry) was used for particle impacts. Considering the measured parameters of the field observation, we used debris-flow density for both approaches. We found that both methods produce the same dimensionless pressure. Given the need for more direct samples (measurements of viscosity,μ_f) with the second method, we derived our non-dimensional impact pressure P^* from impact pressure (P_i), averaged flow velocity (U_m), and debris-flow density (ρ_s) as:

$$P^* = \frac{P_i}{U_m^2 * \rho_s}, \tag{13}$$

P_i is the average impact pressure derived from measurement. The impact-force measurement is the impact pressure multiplied by the area of the impact sensor. This definition is very similar to that used for estimating the impact load of geophysical flows against barriers using a momentum-based approach ($P_i = \beta\rho v^2$, v, the average flow velocity, ρ, the bulk density of flow, β, a dynamic coefficient accounting flow composition and barrier type) (Hungr et al., 1984; Mizuyama, 1979; VanDine, 1996). There is a large amount of work trying to characterize the coefficient from analytical and experimental aspects (e.g., Choi et al., 2017; Zheng et al., 2022). The dynamic coefficient in the proposed formula can range from 0.4 to 17.0 in flume experiments (Choi et al., 2017; Zheng et al., 2022). Some theoretical and experimental investigations have indicated that it is a function of the Froude number $\left(5.3{N_{Fr}}^{-1.5}\right)$ (e.g., Cui et al., 2015; Hübl et al., 2009).

We performed correlation analysis between the non-dimensional pressure and concentration (C, Figure S11 in Supporting Information S1), relative flow depth ($H = h/H_m$, Figure S12 in Supporting Information S1), particle Reynolds number (N_{Re}, Figure S13 in Supporting Information S1), and Froude Number (N_{Fr}, Figures S14 and S15 in Supporting Information S1). For the non-dimensional pressure (P^*), we took the average value of impact pressure (P_i), and particle density was assumed to be a constant (2,650 kg m^{-3}). The Pearson correlation coefficient was used to analyze linear correlations between multiple attributes of the non-dimensional impact pressure and the dimensionless numbers, calculated as follows:

$$R_{XY} = \frac{\mathrm{cov}(X, Y)}{\sigma_X \sigma_Y}, \tag{14}$$

where R_{XY} is the Pearson correlation coefficient between two variables, σ_X and σ_Y are the standard deviation of X and Y, cov(X, Y) is the covariance of X and Y. Concerning the range of values of the Pearson correlation coefficient between X and Y, we can distinguish the following cases: $R_{XY} = 1$, variable Y is perfectly correlated with variable X; $0.8 < R_{XY} < 1$, the strong correlation of variable Y with variable X; $0.3 < R_{XY} < 0.6$, moderate correlation of variable Y with variable X; $0 < R_{XY} < 0.3$, weak correlation of variable Y with variable X; $R_{XY} \approx 0$, no linear correlation of variable Y with variable X.

2.5. Simplified Particle Impact Model

In this section, we developed a simple model based on the fundamental physics of particle-sensor interaction to investigate the relationship between particle impact behavior (PSD) and overall hydrodynamics (e.g., averaged

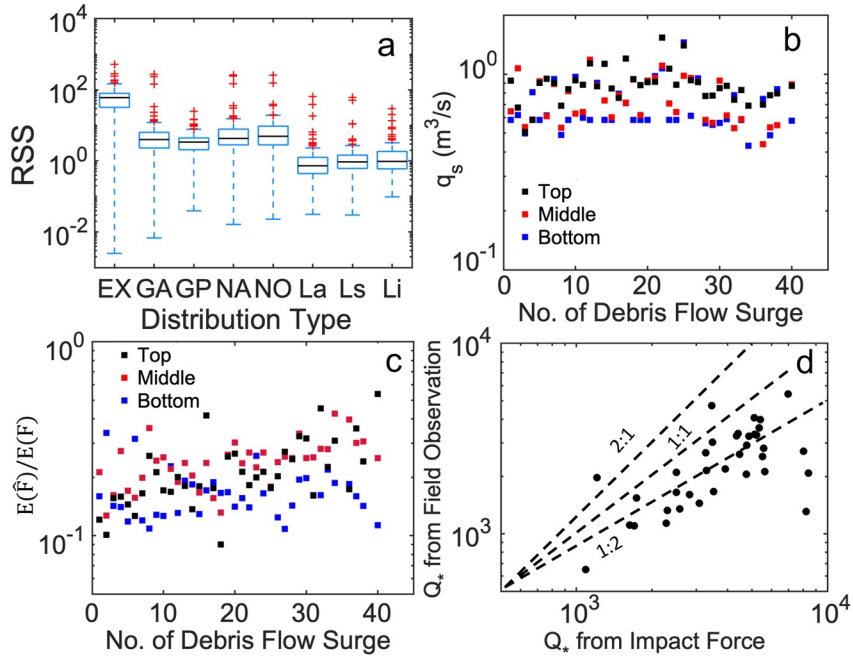

Figure 4. Summary of field measurements, statics, and simulations for the debris flow on 25 August 2004: (a): The residual sum of squares for different distributions used to fit probability density functions: EX: Exponential distribution; GA: Gamma distribution; GP: Generalized Pareto distribution; NA: Nakagami distribution; NO: Normal distribution; La: Log-logistic distribution for all measurements; Ls: Log-logistic distribution for measurements during the debris-flow surge; and Li: Log-logistic distribution for measurements during the intersurge flow. Box with quartiles represents 75% of the data range, the black line represents the mean, and the red cross represents outliers. (b): Estimated sediment flux from field observation for each surge; (c): Estimated particle impact energy ratio ($E(\hat{F})/E(F)$, where $E(\hat{F})$ represents the impact energy of particle and $E(F)$ represents the total energy). (d): Estimated dimensionless discharge from field measurements and a simplified particle impact model over the surface of three impact force sensors.

flow velocity, U_m and sediment flux, q_s) in debris flows. We develop the conceptual model considering a single impact between the sediment particle and sensor. We mainly focused on the high-frequency component of the impact-force signal generated by particle impact with sensors from the flow body. Therefore, we average the theoretical PSD (PSD_m) from the model over the frequency 1 Hz to 2 kHz range that our instruments measure, and equating the equivalent average from field measurements. It should be noted that PSD from field measurements (PSD_f) is a signal form of PSD, which needs to transform to a physical power spectrum to compare with PSD_m (See Text S2 in Supporting Information S1 for details). To quantify the magnitude of debris-flow surges and compare them with other on-site estimations, we assume that the averaged sediment flux over three sensors and depth-averaged sediment concentration represents the entire channel. We estimated the unit dimensionless flow discharge for all debris-flow periods (Q_*) by replacing U_m with estimated averaged particle velocity ($\overline{U}$) from the model in Equation 6. In practice, discharge, especially peak discharge, and total volume are widely used to characterize debris flow events. The dimensionless discharge is more representative than velocity as a non-dimensional variable. We validate our model by comparing Q_* based on field measurements of average surge velocity (U_m from Table S1 in Supporting Information S1) and the particle impact model at the end (Figure 4d).

First of all, we assume the theoretical PSD (PSD_m) is the sum of the impact force radiated over the surface area of the sensor in the y and z-direction for all recorded frequencies (f) and grain diameters (D):

$$\mathrm{PSD}_m(f) = \int_D \int_y \int_z R_{\mathrm{impact}} E_m \, dz \, dy \, dD. \tag{15}$$

R_{impact} is the rate of particle impact per unit volume and grain size:

$$R_{\mathrm{impact}} = \frac{\overline{U} C G(D)}{\overline{V}} = \frac{\rho_s}{\overline{m}} \overline{U} C G(D), \tag{16}$$

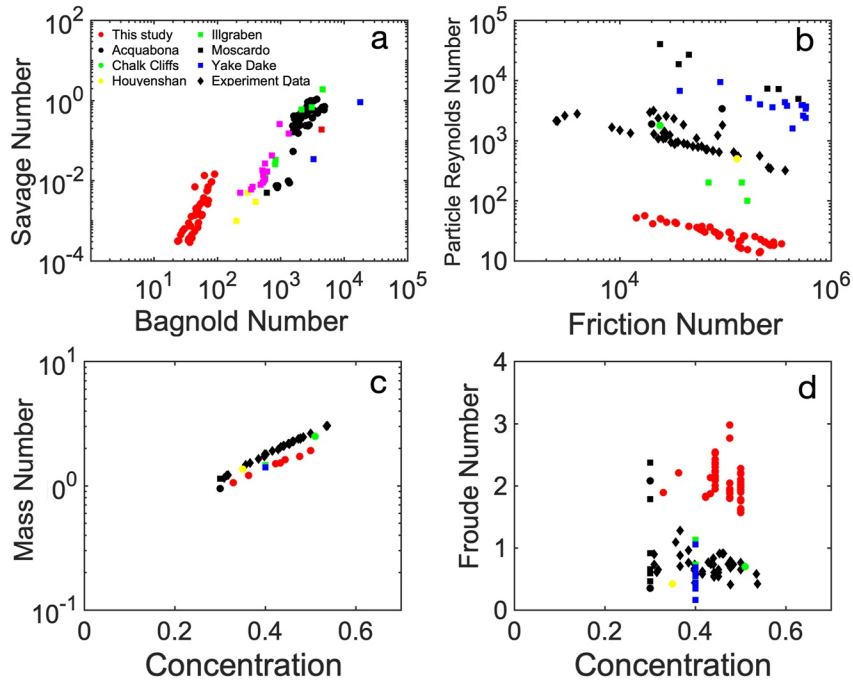

Figure 5. Summary of comparison between field measurements, experiment, and our observation for the debris flow on 25 August 2004: (a–d) Dimensionless number spaces for (a) Savage number and Bagnold number; (b) Particle Reynolds number and friction number; (c) Mass number and sediment concentration; (d) Froude number and sediment concentration with data from debris flows observed at different field sites (Illgraben, Switzerland; Acquabona, Italy; Moscardo, Italy; Chalk Cliffs, USA; Yake Dake, Japan; and Houyenshan, China). All field data from other basins and experiment data are adapted from Lanzoni et al. (2017).

where $\overline{U}$ is the average particle velocity normal to the sensor, C is the sediment concentration, $G(D)$ is grain size distribution, and $\overline{V}$ and $\overline{m}$ are the average particle volume and mass, respectively. Suppose the particle impacts the sensor with impact speed, u_{impact}, at an impact angle, α, to the sensor surface, and we assume the impact is instantaneous. In that case, the measured impact energy is given by (See Text S1 in Supporting Information S1 for details):

$$E_m = (1 - e_b)^2(1 + e_b)m\overline{U}^2. \tag{17}$$

Here, e_b is the basal coefficient of restitution, which is zero for a fully inelastic impact and one for a fully elastic impact. Our sensors are made of stainless steel plate, so $e_b \approx 0.7$. We also assume that grains are spherical and have a uniform grain size, D_{50}:

$$m = \overline{m} = \frac{\pi}{6}\rho_s D_{50}^3. \tag{18}$$

Combining equations from 15–18, we can estimate the PSD_m for different debris-flow periods (See Text S1 in Supporting Information S1 for details):

$$PSD_m(f) = (1 - e_b)^2(1 + e_b)\rho_s AC\overline{U}^3. \tag{19}$$

Here, A is the sensor area. Equation 19 is expected to give an order-of-magnitude estimation of the PSD when the averaged particle velocity $\overline{U}$ and particle concentration C are known.

2.6. Uncertainty Calculation

The uncertainty is used to evaluate the flow velocity, the median grain size (D_{50}), and other data of different groups of debris flows. The uncertainty refers to the uncertainty of the obtained results due to the existence of

errors such as measurement and investigation. In turn, it also indicates the reliability of the results. It is an indicator of the quality of data results. The smaller the uncertainty, the higher the data quality. Given the limited data, the maximum deviation is used to quantify the uncertainty:

$$U_c = \max\left\{ |\overline{A} - A_i|, i = 1, 2, \ldots, n \right\}, \tag{20}$$

where A_i is each data in the data group for which we want to analyze the uncertainty, $\overline{A}$ is the average of the data group, and U_c is the uncertainty of the data group. Based on the average flow velocity of all debris flows (Tables S1 and S2 in Supporting Information S1), the uncertainty using Equation 20 is 5.39 m/s.

3. Results

3.1. Field Observations

In general, field observations indicate debris-flow surges in Jiangjia Ravine are muddy, relatively shallow, and fast-moving, with high sediment concentration (see Movie S1). Surges were usually characterized by a distinguishable front and could be easily detected visually in the impact-force signal using the criteria of Cui et al. (2015). Surge fronts were often characterized by a large number of coarse-grained particles (10 cm) at the flow surface due to grain segregation and were typically over 10 cm deep. Water-rich intersurge flows lacked coarse particles on the flow surface and were characterized by turbulence, waves, and splashes. Debris-flow surges lasted about 8–39 s. The mean velocity of surge fronts ranged from 4.2 to 11.8 m s^{-1} with an average value of around 6.5 m s^{-1} between the two observation sections (Tables S1 and S2 in Supporting Information S1). The flow depth for debris flows was about 0.4–2.0 m, and flow width varied from 2 to 40 m. We estimated discharge and sediment concentration for each surge (Tables S1 and S2 in Supporting Information S1), with discharge ranging from 4. in the last debris-flow period to 840.0 m^3 s^{-1} in the first surge. During all observed debris flow events, sediment concentration was about 51% at the start, reduced to 42% around 1 hr later, and decreased to 33% by the end of the debris-flow event. No clear water flows were observed.

3.2. Impact Force Time Series and Statistics

Field observations indicated no visible sedimentation at the bottom of the sensor during the 19th surge (like the other flows), suggesting conditions at the sensor did not change throughout the debris-flow event. The impact-force measurements from debris-flow surges show some general characteristics, which we illustrate regarding the 19th surge (Figure 3). Impact force data for other selected debris flows are shown in the Figures S1–S4 in Supporting Information S1. Figure 3 shows the impact-force measurements varied from different sensor locations (top, middle, and bottom) and flow magnitudes. No significant fluctuations in the time-averaged mean force were recorded when the force plates were impacted by a debris flow greater than one m. However, the magnitude of high-frequency force components varied by more than 20-fold (Figure 3). Given the significant variation in high-frequency (>5 Hz) force components, we focused on those measurements directly related to grain behavior in debris flows.

While debris flows directly impact the sensor, the impact-force signal ($F(t)$) has a significant fluctuating component $\left(\hat{F}(t)\right)$ with a maximum amplitude that can exceed the median ($\overline{F}(t)$) by several orders of magnitude. Above 80 Hz, power spectra from each surge and sensor decreased quickly (Figures 3I,a, 3II,a, and 3III-a). The general pattern of higher spectral density at lower frequencies is apparent in spectrograms of impact force (Figure 3). When impact-force measurements are separated into groups based on the location of the sensor (top, middle, bottom), the magnitude of high-frequency fluctuations (>5 Hz) usually increases in each group with an increment of the mean impact force (Figures S1–S4 in Supporting Information S1). The low-frequency part (1–5 Hz) has the highest PSD (Figure 3, Figures S5 and S6 in Supporting Information S1). The decomposed signals show that, on average 21%, of the particle impact energy is delivered in the high-frequency region (11%–33% for the top sensor, 13%–43% for the middle sensor, and 1%–53% for the bottom sensor in Figure 4c). Changes in flow depth occurred slowly and persisted over long periods, which would not cause short-duration, large-magnitude fluctuations. However, the responsible specific particle-sensor interactions are challenging to determine from the force-time series alone. The large magnitude impact-force fluctuations and their spectra from granular surges and water-rich intersurge shared similar characteristics (Figures 3I,b, 3II,b, and 3III-b). Granular surge fronts

commonly showed distinct rapid increases in the impact-force signal, but the transition from granular surge to watery intersurge flow sometimes was difficult to determine. Both flow types recorded similarly large impact forces and exhibited instances in which large pulses saturated the measured frequency band (Figure 3).

Probability density functions (PDFs) of normalized impact force for each measured debris flow were right-skewed and decayed slowly with a heavy tail that probability distribution functions with polynomially decreasing upper tails (regularly varying tails) (Alves et al., 2006; McCoy et al., 2013; Pisarenko & Rodkin, 2010) (e.g., Figure 3I-d, 30th surge in Figure 7). The averaged RSS for all distributions with LLD was about 2.04 (La in Figure 4a), which indicates a good fit. The estimated scale parameter for PDFs that fit with LLD varied from 0.02 to 0.23, and the estimated shape parameter, p, ranged from −0.08 to 0.00, with the mean value around −0.01. The results of fitting show a weak positive correlation (RSS, Tables S3–S7 in Supporting Information S1) with measures of event magnitude, such as event-averaged flow depth. When impact-force measurements are plotted by sensor location (top, middle, and bottom), they fit the LLD better than the Generalized Pareto distribution and exponential distribution (Figures 6 and 7). However, the top sensor sometimes has slightly higher variability with a heavier tail than the middle and bottom sensors (e.g., Figures 3I-d and 8). The LLD is usually a better fit for the heavy tail part than for data below the time-averaged mean impact force (Figure 7). We attribute the poor separation of distributions for the three sensor depths to their relatively close spacing (30 cm), and flow depth is an imperfect predictor of impact force in natural debris flows. The normalized impact-force PDFs for surge and intersurge flows overlap and show similar scale and shape parameters within error. Seventy-Six percentage of PDFs from surges have a heavy tail that is over double the time-averaged impact force, while 30% of PDFs from intersurge flows have a heavy tail (Figure 8). Also, the impact-force PDFs for intersurge flows show less variation between the three vertically separated sensors than surges (except the 24th surge, Figure 8). As the time-averaged mean force increases, indicating increasing surge magnitude, the mean and dispersion of the distribution increase, but the type and shape of the distribution only change slightly. The slight increase in the time-averaged mean force from the top to bottom sensor results in stretching the distribution to accommodate the increasing mean and dispersion around the mean, but the overall shape remains the same.

Tables 1 and 2 summarize the Kolmogorov-Smirnov test (KS-Test) results for all 38 debris-flow surges. P_a is the asymptotic p-value, and D_t is the test statistic. H_k is the hypothesis test result in each Kolmogorov-Smirnov test. When $P_a > 0.05$, H_k is equal to zero, indicating that the distributions from surge and intersurge flow are similar, as shown in Figure S9 in Supporting Information S1 (third surge). When $P_a < 0.05$, it is assumed that $H_k = 1$, the distributions from surge and intersurge flow are not similar, such as in channel one (top sensor) and channel three (bottom sensor) in Figure S10 in Supporting Information S1 (12th surge). For the 114 results from the 38 surges, 100 cases show similar surge and intersurge distributions. Sixteen cases (14%) were not similar, of which four were in the top sensor (3.5%), four in the middle sensor (3.5%), and eight in the bottom sensor (7%).

3.3. Flow Dynamics

Overall, debris flows at Jiangjia Ravine are characterized by small N_{Ba} (23.5–90.8) and N_{Sa} (0.0003–0.0146), which suggests a mixed regime between friction and collision for grain-to-grain processes at our study site (Figure 5a). The low N_{Re} (13.6–56.0) of flows at Jiangjia Ravine corresponds to a stress regime dominated by viscous, quasi-static actions with a low degree of turbulence at the particle scale (Figure 5b). Large values of N_f (14,000–340,000) suggest that frictional shear stresses exceed viscous shear stresses. Values of N_m greater than one (Figure 5c) indicate that solid grain dynamics dominate momentum transport in debris flows. All debris-flow surges at our study site are supercritical since the Froude number is higher than one (Figure 5d). There are significant differences between the seven dimensionless parameters from our study site and those determined experimentally by Lanzoni et al. (2017) (Figure 5). The laboratory-generated debris flows from Lanzoni et al. (2017) exhibit collisional regimes ($N_{Sa} > 0.1$ and $N_{Ba} > 450$), while debris flows at Jiangjia Ravine usually show a transitional regime between friction and collision. Lanzoni et al. (2017) results also have higher particle Reynolds numbers (>2,500) and subcritical Froude numbers (<1). Surge development at Jiangjia Ravine is often driven by the transport of medium- and fine-grained sediment within the channel in slurries and non-Newtonian fluids (Cui et al., 2005), which differentiates them from the laboratory debris flows that are coarse-grained. These differences suggest different stress-generating mechanisms causing spatially varied rheology (frictional or collisional) at Jiangjia Ravine than those observed in flume experiments by Lanzoni et al. (2017). Real debris flows from Jiangjia Ravine are generally characterized by an abundance of fine-grained sediment with wide grain

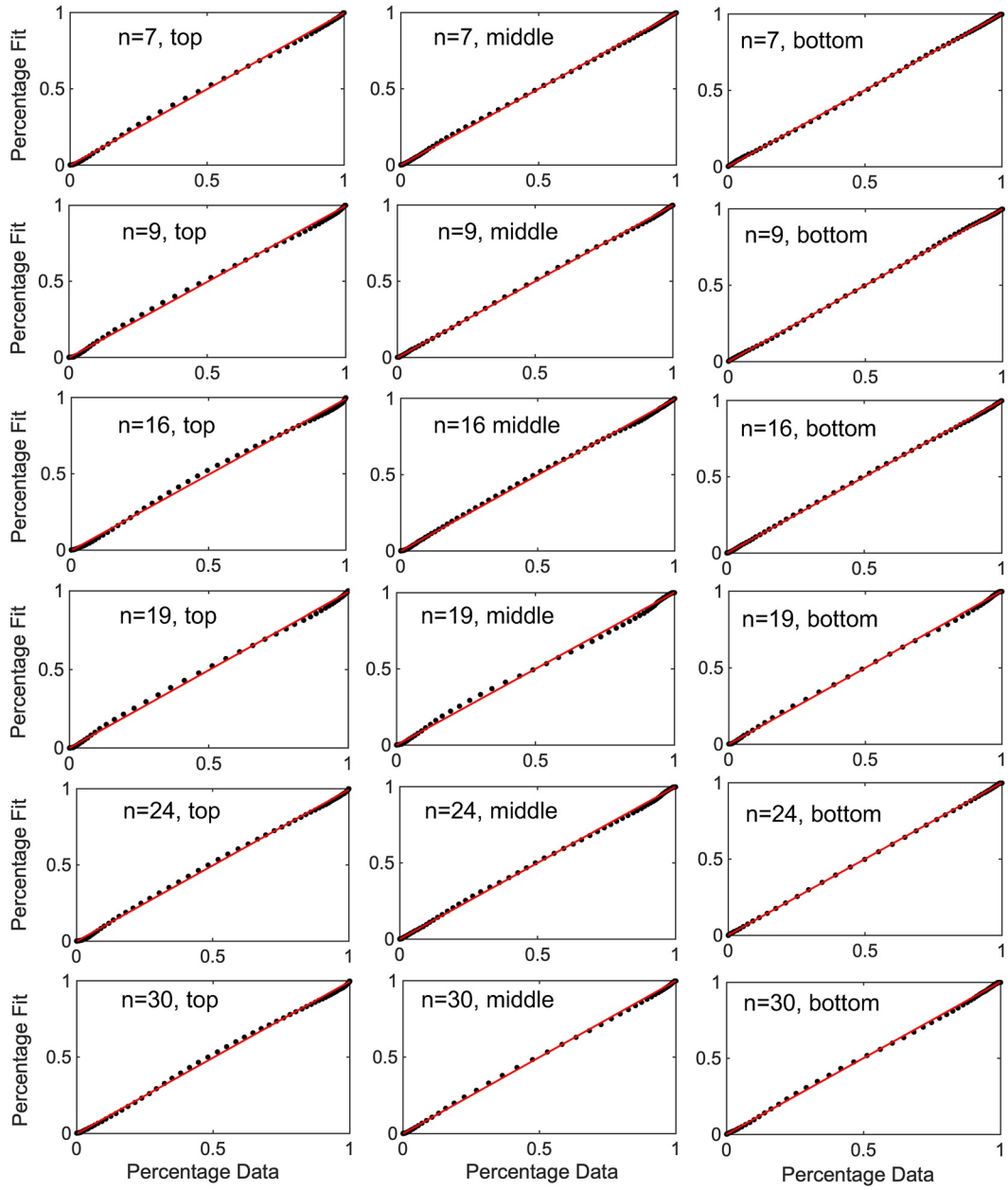

Figure 6. Percentage-percentage plots for debris-flow surges No. 7, 9, 16, 19, 24, and 30 with log-logistic distributions. This visualization allows an assessment of the goodness of fit for both low and high-normalized impact forces from measurements. The red lines represent a 1:1 match between measurements and the fitting function. When the red line and black dots are completely overlapping, the distribution is perfectly fitting to the measurements. Overall, the right top part (percentage fit >0.75 and percentage data >0.75) of the red line fit better than other parts of the line.

size ranges and low turbulence, which may further complicate direct comparisons between our results and the experiments of Lanzoni et al. (2017). Overall, the analysis of dimensionless parameters shows that debris-flow behavior at Jiangjia Ravine differs from that observed in stony debris flows. From the results of the correlation analysis (in Table 3, Figures S11–S15 in Supporting Information S1), the Pearson correlation coefficients for non-dimensional impact pressure P^*, particle Reynolds number, concentration, relative flow depth, and Froude number are 0.1665, 0.0715, 0.1298, and 0.0457, respectively. Non-dimensional impact pressure P^* and particle Reynolds number have the strongest correlation, but all values are less than 0.3. This shows that non-dimensional impact pressure P^* is weakly correlated with all other dimensionless parameters.

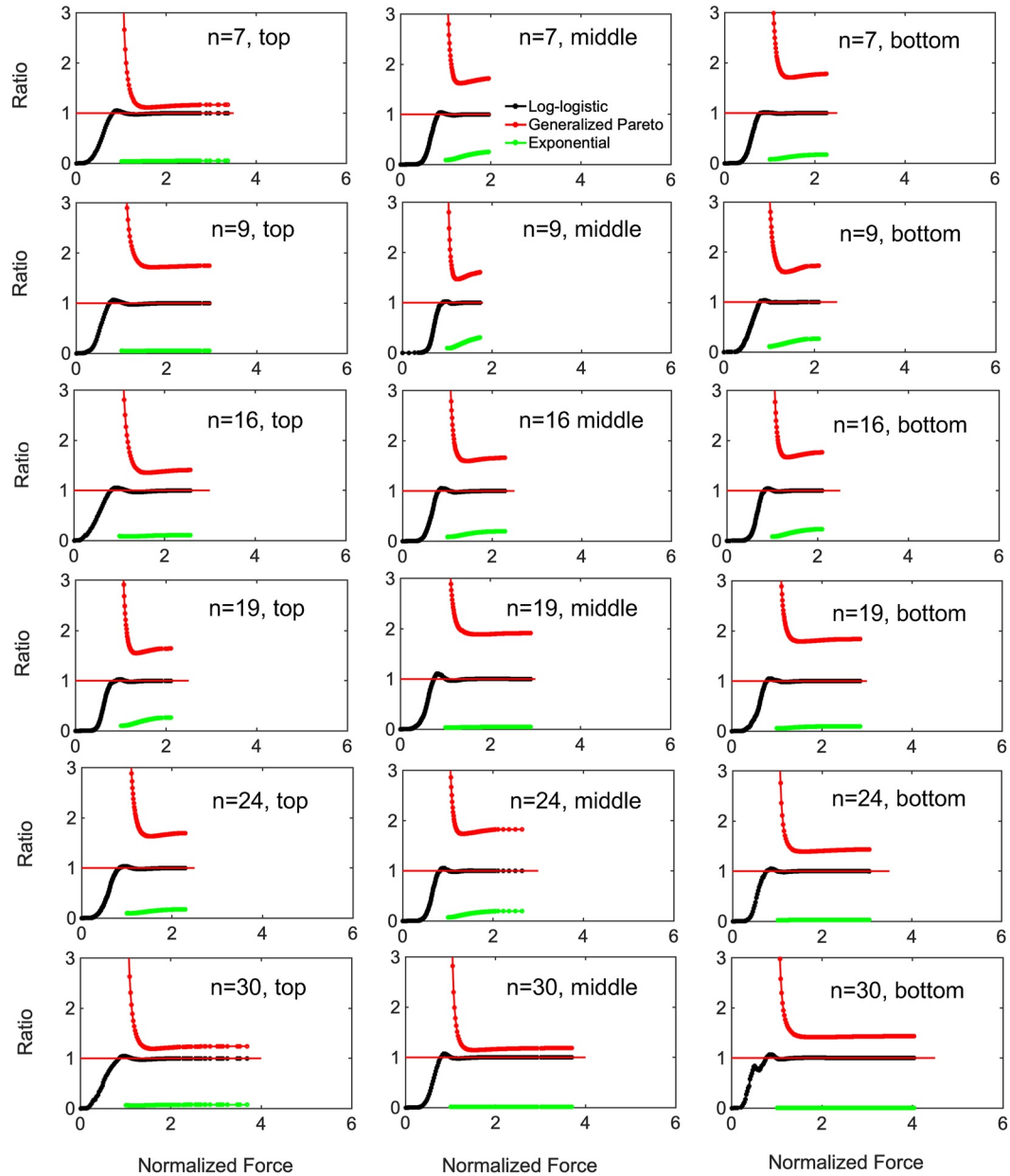

Figure 7. Percentile ratio plots for debris-flow surges No. 7, 9, 16, 19, 24, and 30 fitted with log-logistic distributions, generalized Pareto distributions, and exponential distributions: the ratio equal to one (solid red line) indicates a perfect fitting. The generalized Pareto distributions (the red line with dots) overestimate the impact force. In contrast, the exponential distribution (the green line with dots) significantly underestimates impact force. They have done a slightly better in the heave tail part (normalized force greater than 2). The log-logistic distributions tend to underestimate normalized impact force under one and do a good fitting in the heave tail part, which slightly overestimates the overall impact force.

Non-dimensional discharge Q_* from field observation and Q_* from impact force between different debris flows are approximately linearly related with about 20% error (Figure 4d). The relatively good fit of our model results for debris-flow sediment flux and its vertical variation at Jiangjia Ravine demonstrates that a simple particle impact model can be used to interpret grain-scale behavior in debris flow with real-time impact-force measurements. This cannot be achieved through traditional methods or dimensionless numbers. Based on sediment flux (q_s) over the sensor surface and dimensionless discharge during debris-flow periods (Q_*) from the model, sediment flux is generally higher on the top sensor than on the middle and bottom sensors (Figure 4b). The flux on the top sensor ranges from 0.31 to 0.94 $m^3\ s^{-1}$, and that on the bottom sensor from 0.26 to 0.89 $m^3\ s^{-1}$. The

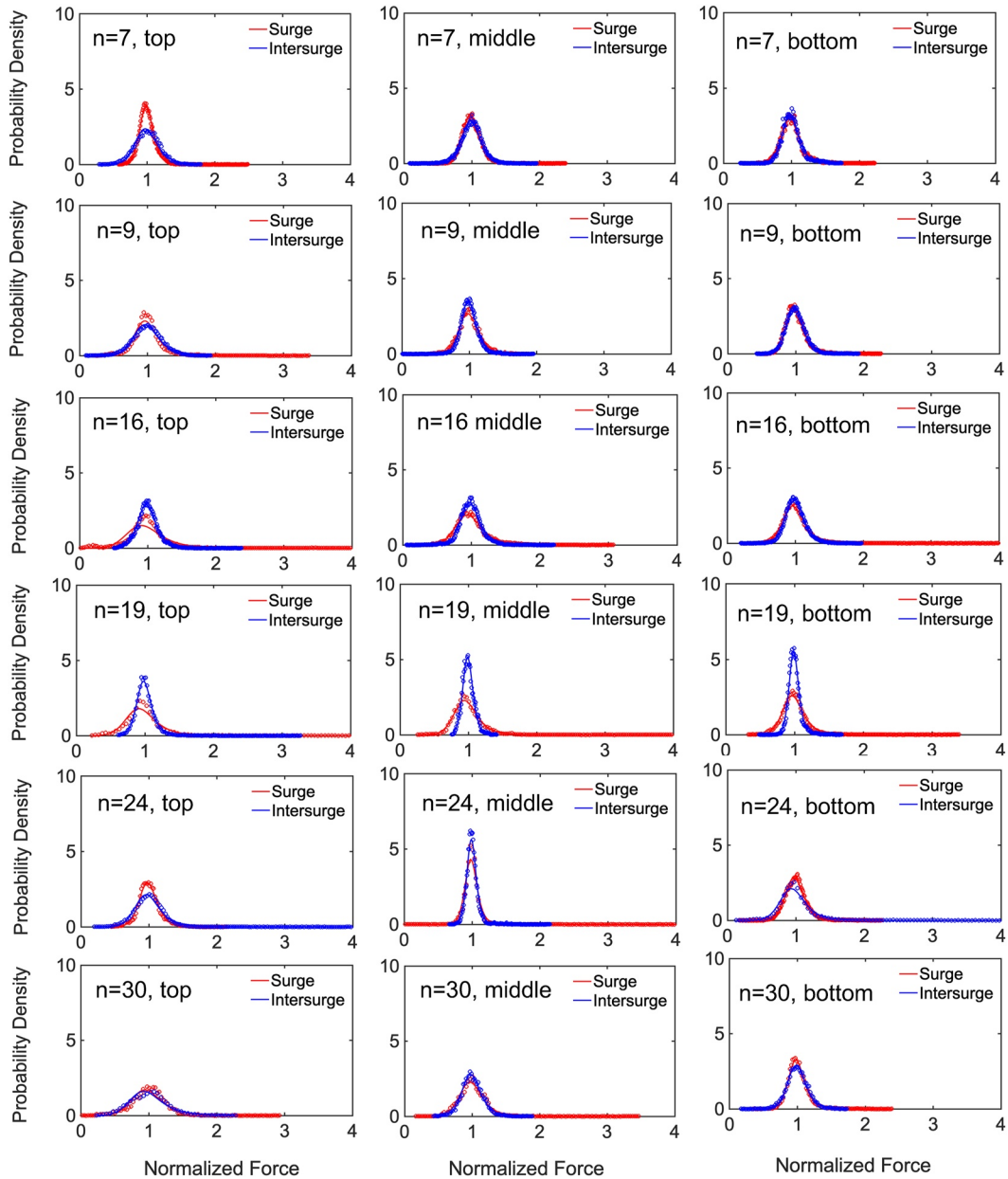

Figure 8. Probability density functions of normalized impact forces for debris-flow surge (red) No. 7, 9, 16, 19, 24, and 30 and following intersurge flows (blue): the red and blue solid lines indicate the fitting lines with log-logistics distributions. The red and blue circles are original field measurements. Except for the middle sensor during the 9th surge, all surges show a heave tail (normalized force greater than 2). In contrast, only intersurge flow after the 16th and 24th surges has shown a heavy tail. In addition, the impact force from the top sensor during intersurge flow after the 19th surge also shows a heavy tail.

maximum dimensionless discharge from the simplified particle impact model is 6,452 for the 19th surge, and the minimum is 670 for the 36th debris-flow period (Figure 4d).

4. Discussion

4.1. Impact Force

The average flow velocity between the two sections is measured by using the method mentioned in Methodology. Then the average flow velocity of all debris flows is calculated (Tables S1 and S2 in Supporting Information S1), so the uncertainty is calculated as 5.39 m/s by Equation 20. Our field measurements show large fluctuations

Table 1
Kolmogorov-Smirnov Test (KS-Test) Results

	Top sensor			Middle sensor			Bottom sensor		
Surge No.	H_k	P_a	D_t	H_k	P_a	D_t	H_k	P_a	D_t
3	0	0.90	0.10	0	0.82	0.11	0	0.39	0.16
4	0	0.43	0.14	0	0.86	0.08	0	0.59	0.16
5	1	0.00	0.26	0	0.06	0.22	1	0.00	0.33
6	0	0.10	0.23	0	0.33	0.12	0	0.27	0.16
7	0	0.08	0.20	0	0.75	0.09	1	0.03	0.20
8	1	0.04	0.20	0	0.29	0.15	0	0.15	0.24
9	0	0.56	0.15	1	0.01	0.27	0	0.33	0.13
10	0	0.44	0.17	0	0.44	0.15	1	0.04	0.24
11	0	0.21	0.19	0	0.11	0.21	0	0.66	0.15
12	1	0.03	0.26	0	0.93	0.09	1	0.01	0.29
13	0	0.24	0.19	0	0.36	0.14	0	0.30	0.19
14	0	0.38	0.16	0	0.51	0.15	0	0.55	0.16
15	0	0.20	0.17	0	0.51	0.18	0	0.20	0.18
16	0	0.16	0.19	0	0.18	0.16	0	0.35	0.15
17	0	0.12	0.21	0	0.80	0.10	0	0.15	0.16
18	0	0.61	0.15	0	0.21	0.18	0	0.28	0.13
19	0	0.49	0.20	0	0.06	0.25	1	0.04	0.23
20	0	0.13	0.21	0	0.19	0.17	0	0.14	0.19
21	1	0.00	0.32	0	0.12	0.20	0	0.55	0.13
22	0	0.70	0.15	0	0.54	0.11	0	0.50	0.15
23	0	0.83	0.11	0	0.94	0.11	0	0.50	0.13
24	0	0.34	0.19	1	0.00	0.36	0	0.92	0.11
25	0	0.38	0.18	0	0.51	0.68	0	0.54	0.17
26	0	0.60	0.14	0	0.24	0.14	0	0.38	0.16
27	0	0.78	0.13	0	0.48	0.13	0	0.69	0.14
28	0	0.62	0.16	0	0.14	0.20	1	0.03	0.19
29	0	0.80	0.14	0	0.37	0.12	0	0.23	0.14

Note. H_k is hypothesis test result, P_a is asymptotic p-value, and D_t is test statistics.

in impact force during debris flows. Similar to the normal force exerted by debris flows (McCoy et al., 2013), large fluctuations are exclusively high-frequency (>5 Hz), higher than the mean impact-force signal (0–5 Hz). We interpret the high-frequency nature of large-magnitude variations due to momentum exchange between particle and sensor by solid-phase impacts. The median grain size (D_{50}) of the three bulk samples, excluding larger clasts and boulders, the D_{50} of the three groups of grain size data are 10, 8, and 10 mm respectively (Figure S16 in Supporting Information S1). Although the diameter of our sampler is small, only 18 cm, it is found through field observation that the grain size in these debris flows is small, and the particle size exceeding 10 cm is rarely seen. The rare instances when larger particles hit the impact sensors do not affect the overall results. When a large particle hits the sensor, the impact-force signal can be eight times greater than the mean impact force caused by slurry pressure (e.g., Figure 3I-b). In contrast, slurry impact changes occurred much more slowly and resulted in long-duration, small-magnitude fluctuations in the signal (e.g., Figure 3II-b). Two sensors nearby may simultaneously show an impulse if a particle is large enough to impact both of them (Figures 3I-b and 3II-b). When the flow depth is larger than 1.0 m, the particle impact energy ratio $E(\hat{F})/E(F)$ increases over time (Figure 4c). Even though the mean impact force resulting from the slurry component provides most of the impact energy (Figure 3II), large magnitude fluctuations (spike pulse) are likely destructive due to the nonlinearity of forces from solid-phase impact. However, our force measurements alone cannot easily discriminate between particle impacts and other grain-scale processes that may also cause force fluctuations.

The probability density functions of normalized impact force were broad but decayed fast with increasing force magnitude due to the large variability exerted by grain-scale processes (Figure 4a). The good fit of the distribution with LLD indicates more variability in impact-force magnitude in natural debris flows than the normal basal force. There is very limited literature on direct impact-force measurements from natural debris flows; most publications focus on basal forces and their distribution. Bermudez and Kotz (2010) found that generalized Pareto distributions well-described distributions of basal force, as did McCoy et al. (2013) with their field-derived data set. In laboratory experiments and simulations, Y. Huang (2017) demonstrated that contact forces in the tail are distributed exponentially. However, when applied to our field measurements, we found that exponential and generalized Pareto distributions under-predict or over-predict the probability of large magnitude fluctuations by orders of magnitude (Figure 7). The heavy tail of debris-flow surges' PDFs also suggests that surges transfer momentum inside the flow primarily through frequent particle-particle interactions (i.e., collisions between grains, Iverson, 1997; Lanzoni et al., 2017). This corresponds to our field observation of high flow density in debris-flow surges and the presence of coarse grains on the flow surface.

As the mean impact force increased, indicating increasing surge magnitude, the shape parameter of the impact-force distribution increased, but it still fitted well with the LLD. An increase in the LLD shape parameter indicates an increased probability of observing large-magnitude impact forces. In this case, debris flow surges with a large magnitude have a high likelihood of extreme impact forces and high destructive potential. Normalized force distributions for both surge and intersurge flow are similar in most cases without the distribution tails based on the Kolmogorov-Smirnov test (86% of cases with Kolmogorov-Smirnov statistic greater than 0.05, see Tables 1 and 2). Only a few cases are different for the entire normalized force distribution, which corresponds with findings for the normal basal force in natural debris flow (McCoy et al., 2013). Overall, the findings imply that the main difference between debris-flow surge and intersurge flow lies in the impact-force distribution, specifically in the heavy tails. In addition, normalized impact-force distributions for the three sensors collapsed

Table 2
Kolmogorov-Smirnov Test (KS-Test) Results

	Top sensor			Middle sensor			Bottom sensor		
Surge No.	H_k	P_a	D_t	H_k	P_a	D_t	H_k	P_a	D_t
30	0	0.47	0.20	0	0.13	0.23	0	0.73	0.13
31	0	0.79	0.13	0	0.35	0.15	0	0.49	0.23
32	0	0.53	0.17	1	0.03	0.23	0	0.67	0.15
33	0	0.10	0.24	0	0.14	0.16	0	0.30	0.18
34	0	0.15	0.24	0	0.43	0.14	0	0.22	0.19
35	0	0.15	0.26	1	0.00	0.77	0	0.28	0.15
36	0	0.79	0.13	0	0.39	0.20	1	0.00	0.24
38	0	0.08	0.27	0	0.72	0.13	0	0.68	0.14
39	0	0.06	0.31	0	0.95	0.08	0	0.32	0.13
40	0	0.18	0.23	0	0.62	0.14	1	0.03	0.27
42	0	0.74	0.17	0	0.15	0.20	0	0.50	0.15

to the same distribution after the impact force normalized by the mean impact force, indicating the similarity of grain-scale dynamics in the debris flow vertical profile.

4.2. Flow Dynamics

The small N_{Ba} (23.5–90.8) and N_{Sa} (0.0003–0.0146) of debris flows at Jianjia Ravine (Figure 5a) is similar to that found at field sites in Houyenshan, China, and Illgraben, Switzerland, while debris flows at other field sites—Acquabona, Italy; Chalk Cliffs, USA; Moscardo, Italy, and Yakedake, Japan—are characterized by large N_{Sa} and N_{Ba}. The differences between the two sets of sites could be attributed to their grain size characteristics and the nature of grain-to-grain processes. The former sites are characterized by the transport of fine-grained material in slurries and a mixed regime of grain-to-grain processes between friction and collision. The latter sites are characterized by more stony debris-flow surges, where a collisional regime dominates. Hence, our field observation and analysis provide new insight into the quantification of impact force for studying debris-flow dynamics, which could help improve understanding of debris-flow behavior elsewhere in the field. Significant differences exist between all six dimensionless numbers from our study site and those determined experimentally by Lanzoni et al. (2017) (Figure 5).

4.3. Relationship Between Flow Dynamics and Impact Force

When we normalized each force measurement for the corresponding impact force, distributions from all events collapsed toward a single distribution. This indicates the fluctuating component responsible for the observed impact-force variability scales with the time-averaged mean force. All distributions can be described by two parameters: a scale and a shape parameter. We estimated the non-dimensional impact pressure and used the Pearson correlation coefficient to analyze correlations between the non-dimensional impact pressure and several dimensionless numbers (concentration, relative flow depth, particle Reynolds number, and Froude number) (Table 3). The Pearson correlation coefficients are smaller than 0.3, indicating a weak correlation. This was a surprise as, intuitively, we were expecting non-dimensional pressure to be strongly correlated with relative flow depth, particle Reynolds number, and Froude number, as has been indicated in previous studies (Cui et al., 2015). According to experiments by Cui et al. (2015), the dynamics coefficients β and $N_{Fr}{}^{-1.5}$ should also show a strong correlation, but our study could not confirm this. This is mainly due to the variability of field observation data and uncertainty in the theoretical basis for data processing and quantification of dimensionless numbers. For example, Zhou and Ng (2010) mentioned that the analysis of dimensionless numbers, such as F^*, which can reflect that reverse segregation, can significantly influence the debris flows mobility (e.g., transport distance and impact area) and the flow regimes. For non-dimensional impact pressure P^*, P_i is the average impact pressure of each surge. Due to strong turbulence in the head of the debris flow, there is a certain amount of noise in the impact pressure measurement (e.g., the noise of channel one of the sixth surge is about 4.5 kPa, Figure S18 in Supporting Information S1), while the tail of the debris flow is almost calm, and the signal-to-noise ratio of the impact pressure is low (reduces from the head of debris flow surge (5.8) to the tail of debris flow surge (0.3), Figure S18 in Supporting Information S1). Concentration has not been directly measured in the field but was derived from other measurement parameters and averaged for each surge. For the Reynolds number, the calculation method of using flow depth as a substitute for grain size also introduces an error. There is also an error associated with the measurement of flow depth by the ultrasonic level gauge due to the strongly turbulent debris flow with mud splashing, typical of Jiangjia Ravine. The weak correlation between P^* and N_{Fr} (or $N_{Fr}{}^{-1.5}$) further shows a gap between the results of the laboratory experiments (e.g., Cui et al., 2015) on debris-flow impact force and the in-field observations (e.g., K. Hu et al., 2011), indicating that results in the laboratory experiments for impact force on barriers may not be simply and fully applied to in-field observations.

Table 3
Pearson Correlation Coefficient Between Variables

	N_{Re} (particle Reynolds number)	C (sediment concentration)	h/H_m (Relative flow height)	N_{Fr} (Froude number)	$N_{Fr}{}^{-1.5}$
P^*	0.1665	0.0715	0.1298	0.0457	0.0529

4.4. Limitations and Implications for Debris-Flow Hazard Mitigation

Our impact-force measurements and simplified particle impact model results are sensitive to impact sensor size, structural deformation of the sensor, and sensor location, all of which contribute to signal noise. Our measurements are mainly subject to high-frequency harmonic noise (greater than 180 Hz) filtered through EMD. Impact force is distributed in each EMD component as a sharp pulse of about 10 s, and this part of the effective signal component is removed in the filtering process. However, there are real signals in the high-frequency range. For example, boulder impact can generate a signal above 500 Hz, which would also have been removed. We cannot systematically measure the impact contact area to quantitatively analyze the sensitivity to impact-force measurements. A large sensor usually has a higher probability of being impacted by particles of different sizes, and signals measured by a large sensor are generally smoother than those measured by a small one that often has more extreme values (Hsu et al., 2014). Deformation of the sensor surface due to solid-phase impact could reduce the impact-force signal generated, underestimating the actual grain impact component (K. Hu et al., 2011). However, there is no easy way to accurately estimate the deformation effect on the measurements. The middle sensor had about a 5% higher noise level than the other two sensors for all debris-flow surges, but this noise does not influence the PSD, and our inverse model results (less than 9%) based on Equation 19. Laboratory studies have shown that the shape of the velocity profile is similar across the flume (Cui et al., 2015; Lei et al., 2018). Still, the magnitude of the velocity reduces close to the channel bank due to wall friction (Kaitna et al., 2014; Schaefer et al., 2010). We assumed no cross-channel difference in velocity profile shape or magnitude, so our estimations of the total volume of dimensionless discharge may be too high.

Several flume experiments have been conducted to investigate impact load distribution (e.g., Cui et al., 2015; Zanuttigh & Lamberti, 2006), and field experiments have been used to validate impact force sensor measurements (e.g., Bugnion, Bötticher, & Wendeler, 2012; K. Hu et al., 2011; Wendeler et al., 2007). However, many of these studies are small or medium-scale controlled experiments that suffer from scaling problems and were designed for stony debris flows. Numerical studies tend to ignore the extreme impact forces caused by large grains (K. Hu et al., 2011; S. Zhang, 1993) or model them using simplified equations to represent them as slurry impacts or particle impacts rather than as a statistical distribution (e.g., He et al., 2016). While the absolute values of impact forces are specific to the Jiangjia Ravine site, the impact-force distribution is potentially portable to other locations that can be tested in future research. The design of control measures and quantitative vulnerability assessment for debris flows usually depends on impact-force estimations as an order of magnitude in most cases (Cui et al., 2015; Thouret et al., 2020). Therefore, our results offer the potential for developing more accurate guidelines for control measure design and vulnerability assessment for high-viscosity debris flows similar to those at Jiangjia Ravine. Finally, our particle impact-based model could be applied to analyze seismic signals, which have been used to monitor landslides, debris flows, and outburst flood processes (e.g., Arattano, 1999; Burtin et al., 2014; Cook et al., 2018).

5. Conclusion

In this study, we presented and analyzed field measurements and observations of 49 debris flow surges at Jiangjia Ravine, China, during an intense rainstorm on 25 August 2004. By analyzing the measured real-time impact-force signals in both the time and frequency domains, the essential characteristics of impact force are determined. Impact-force measurements during debris-flow events show a high-magnitude, high-frequency fluctuating component. We interpreted fluctuating components as resulting from particle-sensor interaction processes. A new dimensionless number is established to describe the impact force, and its correlation with the existing dimensionless parameters is analyzed. Our results accurately estimate the impact-force distribution needed for designing debris-flow control measures. We found that the broad probability density distribution of impact force that resulted from large variability in the impact force was well-described by a LLD. Meanwhile, solid-dominated surges and fluid-dominated intersurge flows have similar impact-force distributions, but surges usually have heavy tails. We estimated flow discharge using a simple particle impact model and real-time impact-force measurements, and it successfully gave us an order-magnitude estimation for the sediment flux. Dimensionless discharges derived from the proposed model are consistent with other field-based flow discharge estimates at Jiangjia Ravine. The field observations and dimensionless analysis indicate that debris flows at Jiangjia Ravine are mostly muddy, with high sediment concentration and intensive grain-grain interaction processes dominated by a mixed rheological regime. We found that a simple particle impact model can explain these impact force signals from our field measurements

and provide support for the hypothesis that grain-scale dynamics are strongly controlled by solid phases in debris flows. Comparing our dimensionless analysis with flume experiments showed systematic differences between field and experimental debris-flow dynamics that should be considered in future flume experiments.

Notation

$\overline{A}$	Average value of given data group (–)
A_i	data point in give data group (–)
C	Sediment concentration (1)
$C_{\max}$	Closet packing sediment concentration (1)
cov(X, Y)	Covariance of variable X and Y (1)
D	Grain diameter (L)
D_t	Test statistic in Kolmogorov-Smirnov test (1)
D_{50}	Median grain size (L)
E	Impact energy (ML^2T^{-2})
E_m	Impact energy for each particle (ML^2T^{-2})
e	Constant coefficient of restitution (1)
e_b	Basal coefficient of restitution (1)
$\tilde{F}$ or $\tilde{F}(f)$	Fourier transform for the impact force (MLT^{-2})
$F(t)$, $F(n)$, $F(i)$	Impact force (MLT^{-2})
$\overline{F}(t)$	Moving median of the impact force (MLT^{-2})
$\hat{F}(t)$	Fluctuating component of the impact force (MLT^{-2})
$Fn(t)$ or $Fn(i)$	Normalized impact force (1)
Δf	Frequency resolution (T^{-1})
$f(Fn(i))$	Predicted value of $Fn(i)$ from the fit distribution (1)
g	Gravitational acceleration (LT^{-2})
$G(D)$	Probability density function of the grain size distribution (L^{-1})
H	Relative flow depth (1)
H_k	Hypothesis test result in Kolmogorov-Smirnov test (1)
H_m	Flow depth (L)
h	Height of the sensor above the bed (L)
I_{x1}	Impact momentum vertical to sensor (MLT^{-1})
m	Particle mass (M)
N	Number of data points (1)
N_{Ba}	Bagnold number (1)
N_{Fr}	Froude number (1)
N_f	Friction number (1)
N_m	Mass number (1)
N_{Re}	Particle Reynolds number (1)
N_{Sa}	Savage number (1)
P	Pore fluid pressure ($ML^{-1}T^{-2}$)
PDF(Fn, μ, p)	Probability density function of impact force (1)
P^*	Non-dimensional impact pressure (1)
P_a	Asymptotic p-value n Kolmogorov-Smirnov test (1)
P_i	Average impact pressure ($ML^{-1}T^{-2}$)
PSD or PSD_f	Power spectral density of the vibration signal ($M^2L^2T^{-3}$)
PSD_m	Theoretical power spectral density ($M^2L^2T^{-3}$)
p	Shape parameter (1)
Q_*	Dimensionless flow discharge (1)
q_s	Sediment flux (L^3T^{-1})
R_{impact}	Rate of particle impact per unit surface area ($L^{-3}T^{-1}$)
R_{XY}	Pearson correlation coefficient (1)
RSS	Residual sum of squares (1)
r	Sensor radius (L)

T	Window length (T)
Δt	Sampling interval (T)
$\overline{U}$	Averaged particle velocity normal to the sensor (LT^{-1})
U_c	Uncertainty of given data group (–)
U_m	Mean velocity of the surge front (LT^{-1})
V	Particle volume (L^3)
v	Average flow velocity (LT^{-1})
u_{impact}	Impact speed (LT^{-1})
$y(\text{Fn}(i))$	Value of the probability to be predicted for point i (1)
α	Impact angle (°)
β	Dynamic coefficient (1)
γ	Shear rate (T^{-1})
θ	Channel gradient (°)
λ	Linear concentration (1)
μ	Scale parameter (1)
μ_f	Viscosity of the interstitial fluid ($ML^{-1}T^{-1}$)
ρ	Bulk density of flow (ML^{-3})
ρ_f	Density of water (ML^{-3})
ρ_s	Density of sediment (ML^{-3})
σ_e	Effective normal basal stress ($ML^{-1}T^{-2}$)
σ	Normal compressive stress ($ML^{-1}T^{-2}$)
σ_X, σ_Y	Standard deviation of variable X and Y (1)

Conflict of Interest

The authors declare no conflicts of interest relevant to this study.

Data Availability Statement

Raw data and Matlab scripts are distributed in Yan and Tang (2022b) https://doi.org/10.6084/m9.figshare.21078136.v5 and Yan and Tang (2022a) https://doi.org/10.6084/m9.figshare.21078154.v2. The data and monitoring video file can be found in Supporting Information S1.

Acknowledgments
We thank three anonymous reviewers, associate Editor (Odin Marc), and editor (Amy East), for their constructive comments. This study was financially supported by the National Natural Science Foundation of China (Grant 42120104002, 42271075, and U21A2008) and the National Key R&D Program of China (2018YFC1505201). Open Access funding enabled and organized by Projekt DEAL.

References

Alves, M. I. F., de Haan, L., & Neves, C. (2006). Statistical inference for heavy and super-heavy-tailed distributions. *Journal of Statistical Planning and Inference*, *193*(1), 213–227.

Arattano, M. (1999). On the use of seismic detectors as monitoring and warning systems for debris flows. *Natural Hazards*, *20*(2), 197–213. https://doi.org/10.1023/A:1008061916445

Arattano, M., & Franzi, L. (2004). Analysis of different water-sediment flow processes in a mountain torrent. *Natural Hazards and Earth System Sciences*, *4*(5/6), 783–791. https://doi.org/10.5194/nhess-4-783-2004

Armanini, A., Capart, H., Fraccarollo, L., & Larcher, M. (2005). Rheological stratification in experimental free-surface flows of granular-liquid mixtures. *Journal of Fluid Mechanics*, *532*(4), 269–319. https://doi.org/10.1017/s0022112005004283

Ashkar, F., & Mahdi, S. (2006). Fitting the log-logistic distribution by generalized moments. *Journal of Hydrology*, *328*(3–4), 694–703. https://doi.org/10.1016/j.jhydrol.2006.01.014

Badoux, A., Graf, C., Rhyner, J., Kuntner, R., & McArdell, B. W. (2009). A debris-flow alarm system for the Alpine Illgraben catchment: Design and performance. *Natural Hazards*, *49*(3), 517–539. https://doi.org/10.1007/s11069-008-9303-x

Bagnold, R. A. (1954). Experiments on a gravity-free dispersion of large solid spheres in a Newtonian fluid under shear. *Proceedings of the Royal Society of London. Series A. Mathematical and Physical Sciences*, *225*(1160), 49–63. https://doi.org/10.1098/rspa.1954.0186

Bel, C., Liébault, F., Navratil, O., Eckert, N., Bellot, H., Fontaine, F., & Laigle, D. (2017). Rainfall control of debris-flow triggering in the Réal Torrent, Southern French Prealps. *Geomorphology*, *291*, 17–32. https://doi.org/10.1016/j.geomorph.2016.04.004

Bennett, G., Molnar, P., McArdell, B., & Burlando, P. (2014). A probabilistic sediment cascade model of sediment transfer in the Illgraben. *Water Resources Research*, *50*(2), 1225–1244. https://doi.org/10.1002/2013WR013806

Berger, C., McArdell, B. W., & Schlunegger, F. (2011a). Direct measurement of channel erosion by debris flows, Illgraben, Switzerland. *Journal of Geophysical Research*, *116*(F1), F01002. https://doi.org/10.1029/2010JF001722

Berger, C., McArdell, B. W., & Schlunegger, F. (2011b). Sediment transfer patterns at the Illgraben catchment, Switzerland: Implications for the time scales of debris flow activities. *Geomorphology*, *125*(3), 421–432. https://doi.org/10.1016/j.geomorph.2010.10.019

Bermudez, P., & Kotz, S. (2010). Parameter estimation of the generalized Pareto distribution—Part I. *Journal of Statistical Planning and Inference*, *140*(6), 1353–1373. https://doi.org/10.1016/j.jspi.2008.11.019

Berti, M., Genevois, R., LaHusen, R., Simoni, A., & Tecca, P. (2000). Debris flow monitoring in the Acquabona watershed on the Dolomites (Italian Alps). *Physics and Chemistry of the Earth - Part B: Hydrology, Oceans and Atmosphere*, *25*(9), 707–715. https://doi.org/10.1016/S1464-1909(00)00090-3

Berti, M., Genevois, R., Simoni, A., & Tecca, P. R. (1999). Field observations of a debris flow event in the Dolomites. *Geomorphology*, *29*(3–4), 265–274. https://doi.org/10.1016/S0169-555X(99)00018-5

Boudraa, A.-O., & Cexus, J.-C. (2007). EMD-based signal filtering. *IEEE Transactions on Instrumentation and Measurement*, *56*(6), 2196–2202. https://doi.org/10.1109/tim.2007.907967

Bugnion, L., Bötticher, A., & Wendeler, C. (2012). Large scale field testing of hillslope debris flows resulting in the design of flexible protection barriers. *Proceedings of 12th Interpraevent Grenoble/France*.

Bugnion, L., McArdell, B. W., Bartelt, P., & Wendeler, C. (2012). Measurements of hillslope debris flow impact pressure on obstacles. *Landslides*, *9*(2), 179–187. https://doi.org/10.1007/s10346-011-0294-4

Burtin, A., Hovius, N., McArdell, B. W., Turowski, J. M., & Vergne, J. (2014). Seismic constraints on dynamic links between geomorphic processes and routing of sediment in a steep mountain catchment. *Earth Surface Dynamics*, *2*(1), 21–33. https://doi.org/10.5194/esurf-2-21-2014

Chang, K., & Liu, S. (2011). Gaussian noise filtering from ECG by Wiener filter and ensemble empirical mode decomposition. *Journal of Signal Processing Systems*, *64*(2), 249–264. https://doi.org/10.1007/s11265-009-0447-z

Choi, C. E., Cui, Y., Liu, L., Ng, C. W. W., & Lourenço, S. (2017). Impact mechanisms of granular flow against curved barriers. *Géotechnique Letters*, *7*(4), 330–338. https://doi.org/10.1680/jgele.17.00068

Chou, H.-T., Chang, Y.-L., & Zhang, S.-C. (2013). Acoustic signals and geophone response of rainfall-induced debris flows. *Journal of the Chinese Institute of Engineers*, *36*(3), 335–347. https://doi.org/10.1080/02533839.2012.730269

Coe, J. A., Kinner, D. A., & Godt, J. W. (2008). Initiation conditions for debris flows generated by runoff at Chalk Cliffs, central Colorado. *Geomorphology*, *96*(3), 270–297. https://doi.org/10.1016/j.geomorph.2007.03.017

Cook, K. L., Andermann, C., Gimbert, F., Adhikari, B. R., & Hovius, N. (2018). Glacial lake outburst floods as drivers of fluvial erosion in the Himalaya. *Science*, *362*(6410), 53–57. https://doi.org/10.1126/science.aat4981

Cui, P., Chen, X., Waqng, Y., Hu, K., & Li, Y. (2005). Jiangjia Ravine debris flows in south-western China. In *Debris-flow hazards and related phenomena* (pp. 565–594). Springer. https://doi.org/10.1007/3-540-27129-5-22

Cui, P., Guo, X., Yan, Y., Li, Y., & Ge, Y. (2018). Real-time observation of an active debris flow watershed in the Wenchuan earthquake area. *Geomorphology*, *321*, 153–166. https://doi.org/10.1016/j.geomorph.2018.08.024

Cui, P., Zeng, C., & Lei, Y. (2015). Experimental analysis on the impact force of viscous debris flow. *Earth Surface Processes and Landforms*, *40*(12), 1644–1655. https://doi.org/10.1002/esp.3744

Dowling, C. A., & Santi, P. M. (2014). Debris flows and their toll on human life: A global analysis of debris-flow fatalities from 1950 to 2011. *Natural Hazards*, *71*(1), 203–227. https://doi.org/10.1007/s11069-013-0907-4

Draper, N. R., & Smith, H. (1998). *Applied regression analysis* (Vol. 326). John Wiley & Sons.

Farin, M., Tsai, V. C., Lamb, M. P., & Allstadt, K. E. (2019). A physical model of the high-frequency seismic signal generated by debris flows. *Earth Surface Processes and Landforms*, *44*(13), 2529–2543. https://doi.org/10.1002/esp.4677

Gao, L., Zhang, L. M., & Chen, H. (2017). Two-dimensional simulation of debris flow impact pressures on buildings. *Engineering Geology*, *226*, 236–244. https://doi.org/10.1016/j.enggeo.2017.06.012

Gardel, E., Sitaridou, E., Facto, K., Keene, E., Hattam, K., Easwar, N., & Menon, N. (2009). Dynamical fluctuations in dense granular flows. *Philosophical Transactions of the Royal Society A: Mathematical, Physical & Engineering Sciences*, *367*(1909), 5109–5121. https://doi.org/10.1098/rsta.2009.0189

Gregoretti, C., Degetto, M., Bernard, M., Crucil, G., Pimazzoni, A., De Vido, G., et al. (2016). Runoff of small rocky headwater catchments: Field observations and hydrological modeling. *Water Resources Research*, *52*(10), 8138–8158. https://doi.org/10.1002/2016WR018675

He, S., Liu, W., & Li, X. (2016). Prediction of impact force of debris flows based on distribution and size of particles. *Environmental Earth Sciences*, *75*(4), 298. https://doi.org/10.1007/s12665-015-5180-2

Heller, V. (2011). Scale effects in physical hydraulic engineering models. *Journal of Hydraulic Research*, *49*(3), 293–306. https://doi.org/10.1080/00221686.2011.578914

Hsu, L., Dietrich, W., & Sklar, L. (2014). Mean and fluctuating basal forces generated by granular flows: Laboratory observations in a large vertically rotating drum. *Journal of Geophysical Research: Earth Surface*, *119*(6), 1283–1309. https://doi.org/10.1002/2013JF003078

Hu, H., Zhou, G. G., Song, D., Cui, K. F. E., Huang, Y., Choi, C. E., & Chen, H. (2020). Effect of slit size on the impact load against debris-flow mitigation dams. *Engineering Geology*, *274*(105), 764. https://doi.org/10.1016/j.enggeo.2020.105764

Hu, K., Wei, F., & Li, Y. (2011). Real-time measurement and preliminary analysis of debris-flow impact force at Jiangjia Ravine, China. *Earth Surface Processes and Landforms*, *36*(9), 1268–1278. https://doi.org/10.1002/esp.2155

Huang, N. E., & Wu, Z. (2008). A review on Hilbert-Huang transform: Method and its applications to geophysical studies. *Reviews of Geophysics*, *46*(2), RG2006. https://doi.org/10.1029/2007RG000228

Huang, Y. (2017). *Random distribution characteristics and calculation of coarse-particles impact force in debris flow* (pp. 1–120). University of Chinese Academy of Sciences. (in chinese).

Hübl, J., Suda, J., Proske, D., Kaitna, R., & Scheidl, C. (2009). Debris flow impact estimation. In *Proceedings of the 11th international symposium on water management and hydraulic engineering* (Vol. 1, pp. 1–5).

Hungr, O., Morgan, G., & Kellerhals, R. (1984). Quantitative analysis of debris torrent hazards for design of remedial measures. *Canadian Geotechnical Journal*, *21*(4), 663–677. https://doi.org/10.1139/t84-073

Hunt, M., Zenit, R., Campbell, C., & Brennen, C. (2002). Revisiting the 1954 suspension experiments of R.A. Bagnold. *Journal of Fluid Mechanics*, *452*, 124–24. https://doi.org/10.1017/s0022112001006577

Iverson, R. M. (1997). The physics of debris flows. *Reviews of Geophysics*, *35*(3), 245–296. https://doi.org/10.1029/97RG00426

Iverson, R. M., Logan, M., LaHusen, R. G., & Berti, M. (2010). The perfect debris flow? Aggregated results from 28 large-scale experiments. *Journal of Geophysical Research*, *115*(F3), F03005. https://doi.org/10.1029/2009jf001514

Iverson, R. M., & Vallance, J. W. (2001). New views of granular mass flows. *Geology*, *29*(2), 115–118. https://doi.org/10.1130/0091-7613(2001)029<0115:NVOGMF>2.0.CO;2

Kaitna, R., Dietrich, W., & Hsu, L. (2014). Surface slopes, velocity profiles and fluid pressure in coarse-grained debris flows saturated with water and mud. *Journal of Fluid Mechanics*, *741*, 377–403. https://doi.org/10.1017/jfm.2013.675

Kean, J. W., Coe, J. A., Coviello, V., Smith, J. B., McCoy, S. W., & Arattano, M. (2015). Estimating rates of debris flow entrainment from ground vibrations. *Geophysical Research Letters*, *42*(15), 6365–6372. https://doi.org/10.1002/2015GL064811

Kean, J. W., McCoy, S. W., Tucker, G. E., Staley, D. M., & Coe, J. A. (2013). Runoff-generated debris flows: Observations and modeling of surge initiation, magnitude, and frequency. *Journal of Geophysical Research: Earth Surface*, *118*(4), 2190–2207. https://doi.org/10.1002/jgrf.20148

Kwan, J. (2012). *Suggestions on design approaches for flexible debris-resisting barriers*. Discussion Note 1/2012. Civil Engineering and Development Department.

Kwan, J., & Cheung, R. (2012). *Supplementary technical guidance on design of rigid debris-resisting barriers*. GEO Report No. 270. Civil Engineering and Development Department.
Lai, V. H., Tsai, V. C., Lamb, M. P., Ulizio, T. P., & Beer, A. R. (2018). The seismic signature of debris flows: Flow mechanics and early warning at Montecito, California. *Geophysical Research Letters*, *45*(11), 5528–5535. https://doi.org/10.1029/2018GL077683
Lanzoni, S., Gregoretti, C., & Stancanelli, L. M. (2017). Coarse-grained debris flow dynamics on erodible beds. *Journal of Geophysical Research: Earth Surface*, *122*(3), 592–614. https://doi.org/10.1002/2016JF004046
Lei, Y., Cui, P., Zeng, C., & Guo, Y. (2018). An empirical mode decomposition-based signal process method for two-phase debris flow impact. *Landslides*, *15*(2), 297–307. https://doi.org/10.1007/s10346-017-0864-1
Li, Y., Liu, J., Su, F., Xie, J., & Wang, B. (2015). Relationship between grain composition and debris flow characteristics: A case study of the Jiangjia Gully in China. *Landslides*, *12*(1), 19–28. https://doi.org/10.1007/s10346-014-0475-z
Lois, G., Lemaître, A., & Carlson, J. M. (2007). Spatial force correlations in granular shear flow. I. Numerical evidence. *Physical Review E*, *76*(2), 021302. https://doi.org/10.1103/PhysRevE.76.021302
Marchi, L., Arattano, M., & Deganutti, A. M. (2002). Ten years of debris-flow monitoring in the Moscardo Torrent (Italian Alps). *Geomorphology*, *46*(1–2), 1–17. https://doi.org/10.1016/S0169-555X(01)00162-3
McArdell, B. W. (2016). Field measurements of forces in debris flows at the Illgraben: Implications for channel-bed erosion. *International Journal of Erosion Control Engineering*, *9*(4), 194–198. https://doi.org/10.13101/ijece.9.194
McArdell, B. W., Bartelt, P., & Kowalski, J. (2007). Field observations of basal forces and fluid pore pressure in a debris flow. *Geophysical Research Letters*, *34*(7), L07406. https://doi.org/10.1029/2006GL029183
McCoy, S. W., Kean, J. W., Coe, J. A., Staley, D. M., Wasklewicz, T. A., & Tucker, G. E. (2010). Evolution of a natural debris flow: In situ measurements of flow dynamics, video imagery, and terrestrial laser scanning. *Geology*, *38*(8), 735–738. https://doi.org/10.1130/G30928.1
McCoy, S. W., Tucker, G. E., Kean, J. W., & Coe, J. A. (2013). Field measurement of basal forces generated by erosive debris flows. *Journal of Geophysical Research: Earth Surface*, *118*(2), 589–602. https://doi.org/10.1002/jgrf.20041
Mizuyama, T. (1979). Estimation of impact force on dam due to debris flow and its problems. *Journal of the Japan Society of Erosion Control Engineering*, *112*, 40–43.
Nagl, G., Hübl, J., & Kaitna, R. (2020). Velocity profiles and basal stresses in natural debris flows. *Earth Surface Processes and Landforms*, *45*(8), 1764–1776. https://doi.org/10.1002/esp.4844
Okano, K., Suwa, H., & Kanno, T. (2012). Characterization of debris flows by rainstorm condition at a torrent on the Mount Yakedake volcano, Japan. *Geomorphology*, *136*(1), 88–94. https://doi.org/10.1016/j.geomorph.2011.04.006
Oppenheim, A. V., Willsky, A. S., Nawab, S. H., & Hernández, G. M. (1997). *Signals and systems*. Pearson Educación.
Parker, G. (1979). Hydraulic geometry of active gravel rivers. *Journal of the Hydraulics Division*, *105*(9), 1185–1201. https://doi.org/10.1061/jyceaj.0005275
Parker, G., Wilcock, P. R., Paola, C., Dietrich, W. E., & Pitlick, J. (2007). Physical basis for quasi-universal relations describing bankfull hydraulic geometry of single-thread gravel bed rivers. *Journal of Geophysical Research*, *112*(F4), F04005. https://doi.org/10.1029/2006JF000549
Pisarenko, M. V., & Rodkin, M. (2010). *Heavy-tailed distributions in disaster analysis*. Springer Science.
Proske, D., Krawtschuk, A., Zeman, O., Scheidl, C., & Chiari, M. (2018). Debris flow impacts on masonry arch bridges. *Proceedings of the Institution of Civil Engineers-Bridge Engineering*, *171*(1), 25–36. https://doi.org/10.1680/jbren.16.00005
Savage, S. B., & Hutter, K. (1989). The motion of a finite mass of granular material down a rough incline. *Journal of Fluid Mechanics*, *199*, 177–215. https://doi.org/10.1017/S0022112089000340
Schaefer, M., Bugnion, L., Kern, M., & Bartelt, P. (2010). Position dependent velocity profiles in granular avalanches. *Granular Matter*, *12*(3), 327–336. https://doi.org/10.1007/s10035-010-0179-6
Scheidl, C., Chiari, M., Kaitna, R., Müllegger, M., Krawtschuk, A., Thomas, Z., & Proske, D. (2013). Analysing debris-flow impact models, based on a small scale modelling approach. *Surveys in Geophysics*, *34*(1), 121–140. https://doi.org/10.1007/s10712-012-9199-6
Song, D., Zhou, G. G., Choi, C. E., & Zheng, Y. (2019). Debris flow impact on flexible barrier: Effects of debris-barrier stiffness and flow aspect ratio. *Journal of Mountain Science*, *16*(7), 1629–1645. https://doi.org/10.1007/s11629-018-5314-6
Stephens, M. A. (1974). EDF statistics for goodness of fit and some comparisons. *Journal of the American Statistical Association*, *69*(347), 730–737. https://doi.org/10.2307/2286009
Suwa, H., Okano, K., & Kanno, T. (2009). Behavior of debris flows monitored on test slopes of Kamikamihorizawa Creek, Mount Yakedake, Japan. *International Journal of Erosion Control Engineering*, *2*(2), 33–45. https://doi.org/10.13101/ijece.2.33
Tang, H., McGuire, L. A., Rengers, F. K., Kean, J. W., Staley, D. M., & Smith, J. B. (2019). Evolution of debris-flow initiation mechanisms and sediment sources during a sequence of post wildfire rainstorms. *Journal of Geophysical Research: Earth Surface*, *124*(6), 1572–1595. https://doi.org/10.1029/2018JF004837
Thouret, J.-C., Antoine, S., Magill, C., & Ollier, C. (2020). Lahars and debris flows: Characteristics and impacts. *Earth-Science Reviews*, *201*, 103003. https://doi.org/10.1016/j.earscirev.2019.103003
VanDine, D. (1996). Debris flow control structures for forest engineering. In *Res. Br., BC Min. For., Victoria, BC, work. Pap* (Vol. 8).
Wang, D., Chen, Z., He, S., Liu, Y., & Tang, H. (2018). Measuring and estimating the impact pressure of debris flows on bridge piers based on large-scale laboratory experiments. *Landslides*, *15*(7), 1331–1345. https://doi.org/10.1007/s10346-081-0944-x
Wang, Y., Yeh, C., Young, H., Hu, K., & Lo, M. (2014). On the computational complexity of the empirical mode decomposition algorithm. *Statistical Mechanics and its Applications*, *400*, 159–167. https://doi.org/10.1016/j.physa.2014.01.020
Welch, P. (1967). The use of fast Fourier transform for the estimation of power spectra: A method based on time averaging over short, modified periodograms. *IEEE Transactions on Audio and Electroacoustics*, *15*(2), 70–73. https://doi.org/10.1109/TAU.1967.1161901
Wendeler, C., Volkwein, A., Roth, A., Denk, M., & Wartmann, S. (2007). Field measurements and numerical modelling of flexible debris flow barriers. *Debris-Flow Hazards Mitig. Mech. Predict. Assess. Millpress, Rotterdam*, 681–687.
Yan, Y., Cui, Y., Guo, J., Hu, S., Wang, Z., & Yin, S. (2020). Landslide reconstruction using seismic signal characteristics and numerical simulations: Case study of the 2017 "6.24" Xinmo landslide. *Engineering Geology*, *270*, 105582. https://doi.org/10.1016/j.enggeo.2020.105582
Yan, Y., Cui, Y., Huang, X., Zhou, J., Zhang, W., Yin, S., et al. (2022). Combining seismic signal dynamic inversion and numerical modeling improves landslide process reconstruction. *Earth Surface Dynamics*, *10*(6), 1233–1252. https://doi.org/10.5194/esurf-10-1233-2022
Yan, Y., Cui, Y., Tian, X., Hu, S., Guo, J., Wang, Z., et al. (2020). Seismic signal recognition and interpretation of the 2019 "7.23" Shuicheng landslide by seismogram stations. *Landslides*, *17*(5), 1–16. https://doi.org/10.1007/s10346-020-01358-x
Yan, Y., & Tang, H. (2022a). Data, analysis code, model for "Deriving debris-flow dynamics from real-time impact-force measurements" [Software]. figshare. https://doi.org/10.6084/m9.figshare.21078154.v1
Yan, Y., & Tang, H. (2022b). Real-time measurement of debris-flow impact force at Jiangjia Ravine, China [Dataset]. figshare. https://doi.org/10.6084/m9.figshare.21078136.v4

Zanuttigh, B., & Lamberti, A. (2006). Experimental analysis of the impact of dry avalanches on structures and implication for debris flows. *Journal of Hydraulic Research*, *44*(4), 522–534. https://doi.org/10.1080/00221686.2006.9521703

Zeng, C., Cui, P., Su, Z., Lei, Y., & Chen, R. (2015). Failure modes of reinforced concrete columns of buildings under debris flow impact. *Landslides*, *12*(3), 561–571. https://doi.org/10.1007/s10346-014-0490-0

Zhang, S. (1993). A comprehensive approach to the observation and prevention of debris flows in China. *Natural Hazards*, *7*(1), 1–23. https://doi.org/10.1007/BF00595676

Zhang, S., Xu, C., Chen, J., & Jiang, J. (2019). An experimental evaluation of impact force on a fiber Bragg grating-based device for debris flow warning. *Landslides*, *16*(1), 65–73. https://doi.org/10.1007/s10346-018-1083-0

Zhang, S., Xu, C., Wei, F., Hu, K., Xu, H., Zhao, L., & Zhang, G. (2020). A physics-based model to derive rainfall intensity-duration threshold for debris flow. *Geomorphology*, *351*, 106930. https://doi.org/10.1016/j.geomorph.2019.106930

Zhang, Z., Walter, F., McArdell, B. W., Chmiel, M., de Haas, T., & He, S. (2021). Insights from the particle impact model into the high-frequency seismic signature of debris flows. *Geophysical Research Letters*, *48*(1), e2020GL088994. https://doi.org/10.1029/2020gl088994

Zhang, Z., Walter, F., McArdell, B. W., de Haas, T., Wenner, M., Chmiel, M., & He, S. (2021). Analyzing bulk flow characteristics of debris flows using their high frequency seismic signature. *Journal of Geophysical Research: Solid Earth*, *126*(12), e2021JB022755. https://doi.org/10.1029/2021jb022755

Zhao, H., Yao, L., You, Y., Wang, B., & Zhang, C. (2018). Experimental study of the debris flow slurry impact and distribution. *Shock and Vibration*, *2018*, 1–15. https://doi.org/10.1155/2018/5460362

Zheng, H., Shi, Z., de Haas, T., Shen, D., Hanley, K. J., & Li, B. (2022). Characteristics of the impact pressure of debris flows. *Journal of Geophysical Research: Earth Surface*, *127*(3), e2021JF006488. https://doi.org/10.1029/2021jf006488

Zhou, G. G. D., & Ng, C. W. W. (2010). Numerical investigation of reverse segregation in debris flows by DEM. *Granular Matter*, *12*(5), 507–516. https://doi.org/10.1007/s10035-010-0209-4